



REVIEW OPEN ACCESS

Recent Progress in Photocathode Interface Engineering for Photoelectrochemical CO₂ Reduction Reaction to C₁ or C₂+ Products

Jae Hak Kim¹ | Sung Hyun Hong¹ | Sang Hyun Ahn²  | Soo Young Kim¹ 

¹Department of Materials Science and Engineering, Korea University, Seoul, Republic of Korea | ²School of Chemical Engineering and Material Science, Chung-Ang University, Seoul, Republic of Korea

Correspondence: Sang Hyun Ahn (shahn@cau.ac.kr) | Soo Young Kim (sooyoungkim@korea.ac.kr)

Received: 8 February 2024 | **Revised:** 9 June 2024 | **Accepted:** 11 August 2024

Funding: This work was supported by the National Research Foundation of Korea (NRF), funded by the Korean government (2022M3H4A1A01012712, 2022M3H4A1A04096380).

Keywords: cocatalysts engineering | defect engineering | interface engineering | junction engineering | nanostructure engineering | photoelectrochemical CO₂ reduction

ABSTRACT

Photoelectrochemical (PEC) systems harness light absorption to initiate chemical reactions, while electrochemical reactions facilitate the conversion of reactants into desired products, ensuring more efficient and sustainable energy conversion in PECs. Central to optimizing the performance of PECs was the pivotal role played by interface engineering. This intricate process involves manipulating material interfaces at the atomic or nanoscale to enhance charge transfer, improve catalytic activity, and address limitations associated with bulk materials. The careful tuning of factors such as band gap, surface energy, crystallinity, defect characteristics, and structural attributes through interface engineering led to superior catalytic efficiency. Specifically, interface engineering significantly enhanced the efficiency of semiconductor-based PECs. Engineers strategically designed heterojunctions and manipulated catalyst surface properties to optimize the separation and migration of photogenerated charge carriers, minimizing recombination losses and improving performance overall. This review categorizes the discussion into four sections focusing on the interface engineering of PECs, providing valuable insights into recent research trends. Overall, the synergy between PECs and interface engineering holds tremendous promise for advancing renewable energy technologies and addressing environmental challenges by offering innovative solutions for sustainable energy conversion and storage.

1 | Introduction

As industrialization increases worldwide, the number of artificially generated greenhouse gases has risen, continuing to exacerbate climate change [1–3]. Efforts to reduce carbon dioxide (CO₂), the primary contributor to this issue, are intensifying. Despite a temporary decline in global CO₂ emissions due to

the COVID-19 pandemic in 2020, 2021 saw record-high carbon emissions of approximately 36.1 GtCO₂, a 6.3% increase year-on-year [4]. The 2021 IPCC report states that the remaining carbon budget to limit anthropogenic warming to 1.5°C and 2°C above pre-industrial levels, starting from 2020, is 400 GtCO₂ and 1,150 GtCO₂, respectively [5]. Addressing climate change urgently requires innovative solutions [6].

Jae Hak Kim and Sung Hyun Hong contributed equally to this work.

This is an open access article under the terms of the [Creative Commons Attribution](https://creativecommons.org/licenses/by/4.0/) License, which permits use, distribution and reproduction in any medium, provided the original work is properly cited.

© 2025 The Author(s). *Exploration* published by Henan University and John Wiley & Sons Australia, Ltd.

TABLE 1 | Standard reduction potentials of the electrochemical CO₂RR in aqueous solution at pH7.

Products	Reactions	Standard reduction potential [V vs. NHE]
Carbon monoxide (CO)	$\text{CO}_2 + 2\text{H}^+ + 2\text{e}^- \rightarrow \text{CO} + \text{H}_2\text{O}$	−0.53
Methane (CH ₄)	$\text{CO}_2 + 8\text{H}^+ + 8\text{e}^- \rightarrow \text{CH}_4 + 2\text{H}_2\text{O}$	−0.24
Formic acid (HCOOH)	$\text{CO}_2 + 2\text{H}^+ + 2\text{e}^- \rightarrow \text{HCOOH}$	−0.61
Methanol (CH ₃ OH)	$\text{CO}_2 + 6\text{H}^+ + 6\text{e}^- \rightarrow \text{CH}_3\text{OH} + \text{H}_2\text{O}$	−0.38
Ethylene (C ₂ H ₄)	$2\text{CO}_2 + 12\text{H}^+ + 12\text{e}^- \rightarrow \text{C}_2\text{H}_4 + 4\text{H}_2\text{O}$	0.06
Ethanol (C ₂ H ₅ OH)	$2\text{CO}_2 + 12\text{H}^+ + 12\text{e}^- \rightarrow \text{C}_2\text{H}_5\text{OH} + 3\text{H}_2\text{O}$	0.08
Ethane (C ₂ H ₆)	$2\text{CO}_2 + 14\text{H}^+ + 14\text{e}^- \rightarrow \text{C}_2\text{H}_6 + 4\text{H}_2\text{O}$	−0.27
Acetic acid (CH ₃ COOH)	$2\text{CO}_2 + 8\text{H}^+ + 8\text{e}^- \rightarrow \text{CH}_3\text{COOH} + 2\text{H}_2\text{O}$	−0.30
Isopropanol (C ₃ H ₇ OH)	$3\text{CO}_2 + 18\text{H}^+ + 18\text{e}^- \rightarrow \text{C}_3\text{H}_7\text{OH} + 5\text{H}_2\text{O}$	−0.31

To meet this challenge, various technologies have been developed to convert CO₂ into industrially useful chemicals, utilizing methods such as electrochemical reduction (ECR) [7–11], photochemical reduction (PCR) [12–16], and photoelectrochemical (PEC) reduction [17, 18]. However, significant obstacles remain—CO₂ molecules are thermodynamically stable and require considerable electrochemical overpotential for reduction. Besides, in aqueous electrolysis systems, the ECR of CO₂ competes with the hydrogen evolution reaction (HER), necessitating the suppression of the latter to enhance the catalytic activity of the CO₂ reduction reaction (CO₂RR). As depicted in Table 1, ECR involves a complex reaction mechanism, producing a range of hydrocarbon compounds and potential selectivity issues [19, 20]. Product selectivity depends on the adsorption and activation energy of intermediates on the catalyst's surface. For instance, HCOOH can be selectively produced through the formation of *OCHO, while *COOH is a key intermediate in the formation of CO [21]. The formed *COOH intermediate undergoes protonation to create a *CO intermediate, which then desorbs as CO. Besides HCOOH, the reaction mechanism for other hydrocarbon products involves the *CO intermediate [20, 21]. Cu's unique ability to support the formation of C₂₊ products via the two-electron reduction of CO₂ is due to its distinctive properties: negative adsorption energy for the *CO intermediate and positive adsorption energy for the *H intermediate [22]. The *CO intermediate is pivotal in CO₂ ECR, impacting C–C coupling reactions and opening pathways for C₂₊ product formation [23].

Since the first PEC study achieved CO₂RR using a p-GaAs photoelectrode in 1978, sustained efforts have been made to convert photo-driven CO₂ into solar fuel across various fields [24]. PEC CO₂RR has advantages over ECR, including utilizing the photovoltage generated by semiconductor photoelectrodes, reducing system complexity, and partially offsetting the electrical energy required for CO₂RR. Also, accelerated charge separation due to bias-induced band bending enables higher production rates than PCR. PEC cells typically comprise a photoactive semiconductor electrode (photoelectrode), an electrolyte, and a counter electrode with a metal electrode catalyst or a second photoelectrode. The CO₂RR occurs at the cathode, while water oxidation occurs at the anode, with the photoelectrode as either or both [25–27]. In PEC, each electrode can optimize catalyst efficiency based on factors such as bandgap, surface energy, crystallinity, defect characteristics, and structural attributes. Interface engineering is

a promising approach to overcoming the limitations observed in existing bulk materials.

To the best of our knowledge, while several papers have addressed research developments in PEC CO₂RR, comprehensive reviews specifically focusing on interface engineering of photocathodes for producing C₁ or C₂₊ products in PEC CO₂RR are still lacking. As illustrated in Figure 1A, this review is divided into four sections: cocatalyst engineering (plasmonic noble metal and non-noble metal), junction engineering, nanostructure engineering, and defect engineering—from an interface perspective. These sections provide insights into recent research trends in this field of interface engineering of photocathodes for PEC CO₂RR. Additionally, the objective is to compare products generated by PEC, categorizing them into C₁ and C₂₊, and to offer insights into future research directions. Through this article, we aspire to contribute to the advancement of PEC technology grounded in interface engineering, with the ultimate goal of achieving carbon neutrality.

2 | Basics of PEC CO₂RR

2.1 | Principles of PEC CO₂RR

PEC systems offer promising avenues for CO₂RR using solar energy [28]. In a fundamental approach, photocathodes utilizing p-type semiconductor materials harness solar energy to generate photovoltage, serving as the primary driving force to counter the necessary potential for CO₂RR. A standard three-electrode PEC CO₂RR system consists of a p-type semiconductor photocathode for CO₂RR, an n-type semiconductor photoanode for the oxygen evolution reaction (OER), and a reference electrode. Immersing a p-type semiconductor photocathode in a CO₂-saturated aqueous electrolyte creates a semiconductor–electrolyte interface. The difference in Fermi levels across this interface induces a built-in electric field, causing the semiconductor's energy bands to bend downward. Upon light absorption, electron–hole pairs (e[−]/h⁺ pairs) are generated by the promotion of an electron from the semiconductor's valence band (VB) to the conduction band (CB), which then separate into free carriers. Photogenerated electrons from the photoanode migrate to the photocathode, while photogenerated holes transfer from the photocathode to the photoanode. This organized movement of electrons and holes involves the

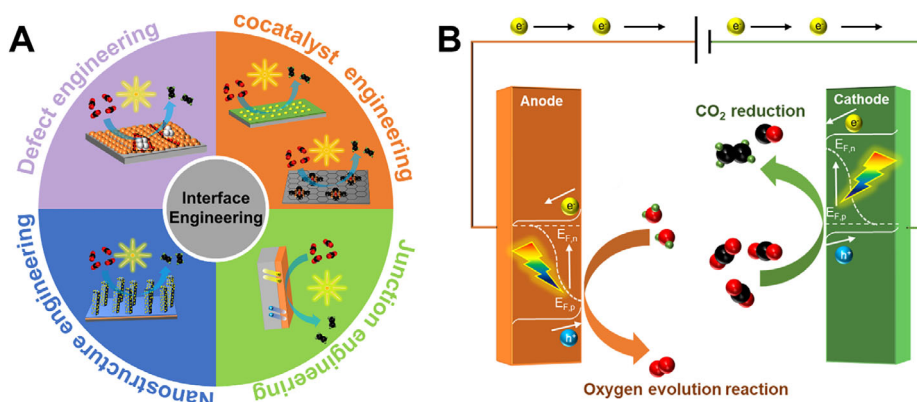


FIGURE 1 | (A) Schematic of interface engineering strategies categorized into four sections. (B) Schematic illustration of basic principles of PEC CO₂RR.

participation of electrons in the CO₂RR and holes in the OER at the interface between the electrode and the electrolyte [19, 29]. A schematic principle of PEC CO₂RR is depicted in Figure 1B.

2.2 | Mechanism for CO₂RR

The molecular structure of CO₂ is highly stable, requiring relatively high energies for C=O activation of approximately 800 kJ mol⁻¹ [30]. The CO₂RR involves several steps, including CO₂ adsorption, CO₂ radical anion formation, key reaction intermediates via proton-coupled electron transfer (PCET), and the formation of desired products. To complete these steps, the high energy barriers of each step must be overcome, which necessitates the application of an additional external potential. As shown in Table 1, distinct numbers of multi-protons and electrons are necessary to generate varying products. As depicted in Figure 2, CO₂ is adsorbed onto the surface of the catalyst and receives an electron to form the CO₂ radical anion. Reaction intermediates such as *OCHO or *COOH are generated through the initial PCET process. For *OCHO intermediates, the oxygen atoms of CO₂ bind to the surface of the catalyst, while the carbon atom is protonated. Through further PCET, either HCOOH or HCOO⁻ is produced, depending on the pH. For *COOH intermediates, the carbon atom of CO₂ binds to the surface of the catalyst. The subsequent PCET process leads to the formation of *CO intermediates. If the desorption energy of *CO is low, *CO desorption is favored, resulting in the formation of CO products. Conversely, if the *CO intermediates bind strongly to the catalyst surface, the reaction pathway diverges into the C₁ pathway and the C₂₊ pathway. In the C₁ pathway, a series of multi-step PCET processes are carried out on the *CO intermediates, resulting in the formation of various C₁ products, such as CH₄, HCHO, and CH₃OH, depending on the binding strength. In contrast, in the C₂₊ pathway, CO dimerization leads to the formation of C=C coupling, followed by a multi-step PCET reaction, resulting in C₂₊ products such as C₂H₄, C₂H₅OH, and C₃H₇OH.

2.3 | In Situ Analysis for CO₂RR

In situ analysis represents a crucial tool for elucidating the underlying factors behind product formation, quantifying product yields, and formulating precise conclusions regarding reaction

sites [31]. This technique is particularly invaluable when dealing with unstable products/species or intricate multistep reaction pathways. In the case of CO₂RR, comprehending the reaction mechanism involving multiple PCET processes poses a challenge. A fundamental understanding of how the catalyst surface interacts with reactive species during the CO₂RR remains elusive. Consequently, numerous in situ techniques have been employed to address these knowledge gaps.

In situ Raman spectroscopy has proven to be a valuable tool for elucidating structural changes in CO₂, identifying intermediate products present on electrode surfaces, and pinpointing catalytic active sites on catalyst surfaces [32]. As illustrated in Figure 3A, a specialized cell was developed, integrating an in situ Raman spectroscopy setup, to facilitate the investigation of (photo)electrochemical CO₂RR. This spectroscopy reveals that structural or compositional changes were predominantly observed on various catalyst surfaces during the CO₂RR.

In situ X-ray absorption spectroscopy (XAS) is also a useful tool for identifying the compositional and structural dynamics of catalysts during (photo)electrochemical CO₂RR [33]. XAS analysis is based on the concept of a specific absorption edge, which is further delineated into two distinct regions. The X-ray absorption near edge structure (XANES) examines the 50 eV vicinity near the absorption edge, while the extended X-ray absorption fine structure (EXAFS) explores the region extending from a few hundred to approximately 1000 eV beyond the edge. XANES is particularly sensitive to the oxidation state of the X-ray absorbing atom and its geometric arrangement relative to the surrounding atoms [34, 35]. On the other hand, EXAFS provides insights into the radial distribution of electron density around the absorbing atom, offering valuable information about the bond length and coordination number [36]. As a result, in situ XAS measurements, conducted using a specialized cell as depicted in Figure 3B, enable the observation of changes in the oxidation state and coordination environment of catalysts during CO₂RR.

In situ electron paramagnetic resonance (EPR) spectroscopy, as illustrated in Figure 3C, is an effective tool for identifying intermediate radicals, such as the CO₂ radical anion, during CO₂RR [33]. The utilization of a spin-trapping agent, such as *N*-tert-butyl- α -phenylnitrone [33] and α -phenyl *N*-tert-butyl nitrone

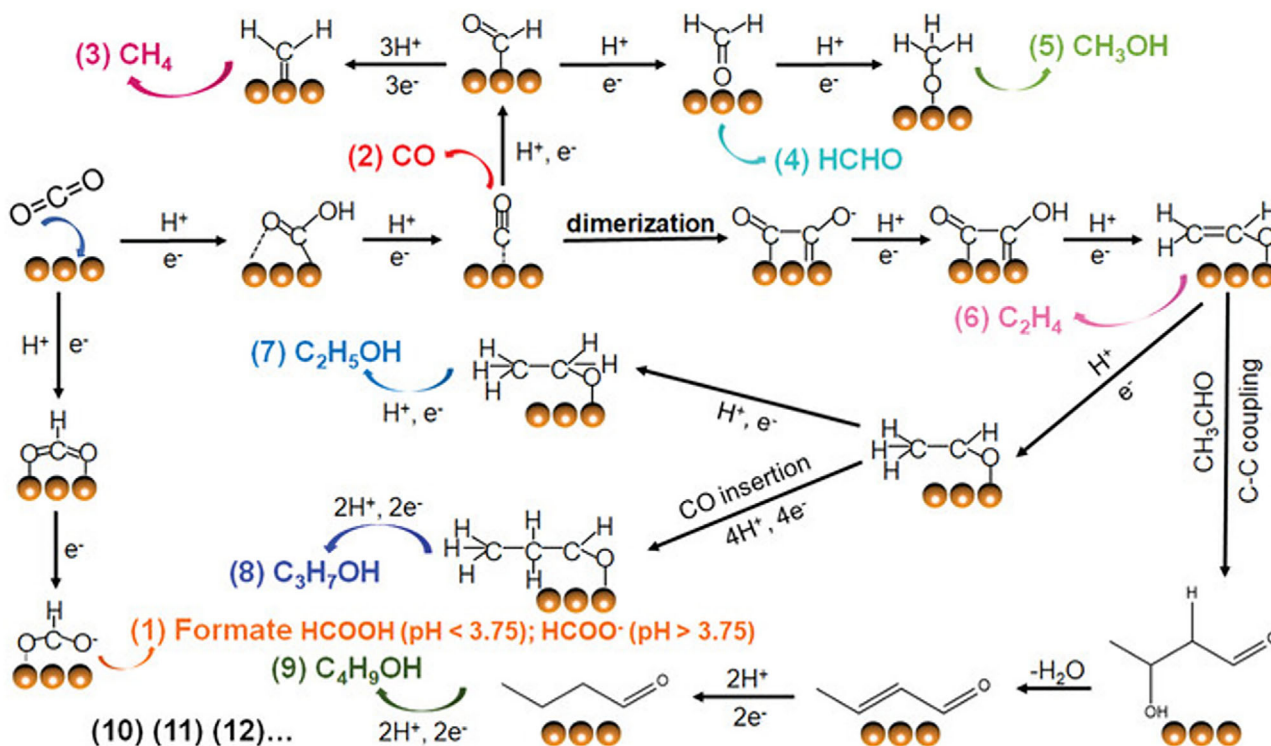


FIGURE 2 | Schematic illustration of the potential pathway for CO_2RR to C_1 and C_{2+} products. Reproduced with permission [30]. Copyright 2022, John Wiley and Sons.

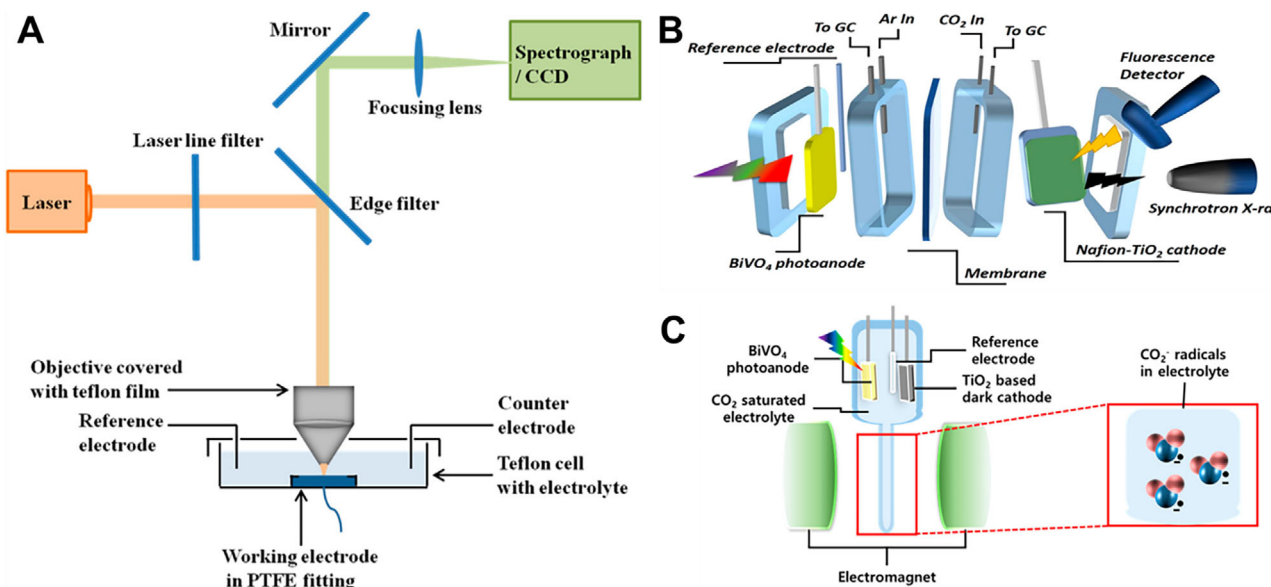


FIGURE 3 | Schematic illustration of specialized cells for in situ analysis corresponding to (A) in situ Raman spectroscopy (B) in situ X-ray absorption spectroscopy (C) in situ electron paramagnetic resonance spectroscopy. Reproduced with permission [32]. Copyright 2017, American Chemical Society. Reproduced with permission [33]. Copyright 2019, American Chemical Society.

[37], facilitates the trapping and detection of these intermediate radicals. Once the intermediate radical-trapping agent complex is constructed, the EPR signal is detected through the unpaired electrons of the intermediate radicals. Therefore, this spectroscopy demonstrates the formation of the intermediate radicals, confirming the occurrence of (photo)electrochemical CO_2RR at the electrode.

3 | Interface Engineering of Photocathodes for PEC CO_2RR

3.1 | Cocatalyst Engineering

Bare semiconductor surfaces typically lack electrocatalytic activity, making it challenging for them to interact effectively with

CO₂ molecules [29]. Integrating appropriate cocatalysts with semiconductor materials is crucial for enhancing surface catalytic conversion, reducing the overpotential of the reaction, and facilitating the transfer of photoinduced charge carriers to surface reactants [38]. This integration accelerates surface reaction kinetics and improves PEC activity and selectivity. Consequently, the efficacy of this integration is contingent upon meticulous cocatalyst selection, the establishment of robust semiconductor-cocatalyst interfaces, and the assurance of their uniform distribution across the semiconductor surface [29]. This section is devoted to the categorization of cocatalysts for PEC CO₂RR into two distinct groups: plasmonic noble metals and non-noble metals. Plasmonic noble metals are distinguished by their surface plasmon resonance properties, which elucidate their optical effects on PEC CO₂RR. In contrast, non-noble metal cocatalysts are primarily characterized by their electrochemical catalytic activity and electron transfer capabilities.

3.1.1 | Plasmonic Noble Metal

Plasmonic noble metal cocatalysts incorporate noble metals like Ag and Au, known for their abundance of free-mobility electrons [39]. Surface plasmon resonance in these cocatalysts originates from the collective oscillations of nanostructures and nanogaps under intense electromagnetic radiation [40–42]. Such resonance, characterized by incident light interacting with the cocatalyst, enhances the redistribution and conversion of light energy through the re-emission of plasmon-induced light, non-radiative decay to excited carriers (hot electrons and holes), and thermal effects over specific timescales [39].

Regarding PEC reactions, the size effect of plasmonic materials becomes significant, with plasmonic noble metal nanostructures improving light absorption, catalytic activity, selectivity, and efficiency [43–47]. Hence, plasmonic noble metal cocatalysts, by exciting surface plasmons, could harness broad-spectrum sunlight, producing high-energy hot carriers that facilitate PEC CO₂RR.

For example, Liu et al. designed a CuBi₂O₄ inverse opal photocathode modified with plasmonic Ag nanoparticles (Ag NPs) using a sacrificial template method (CuBi₂O₄ IOs-Ag) [48]. The 3D-ordered structure of CuBi₂O₄ inverse opal enabled higher mass transfer rates and light harvesting efficiency. Furthermore, incorporating Ag NPs significantly enhanced the surface charge distribution by forming an ohmic contact with CuBi₂O₄. The CuBi₂O₄ IOs-Ag photocathodes showed notable improvements in selectivity for CO production, achieving a faradaic efficiency for CO (FE_{CO}) of 92% at 0.2 V vs. reversible hydrogen electrode (RHE), which is 1.6 times greater than that of the pristine CuBi₂O₄ thin film. Wang et al. prepared n⁺p[−] Si coated with a TiO₂ interlayer and coupled it with plasmonic Au NPs to fabricate photocathodes (Au/TiO₂/n⁺p[−] Si) for PEC CO₂RR to CO [49]. A schematic illustration of the synthesis method is depicted in Figure 4A. Initially, a TiO₂ layer was deposited on the micro-pyramid Si surface using an ALD process, after which Au NPs were fabricated on top of the TiO₂ layer through an electrodeposition method. The Au/TiO₂/n⁺p[−] Si photocathodes exhibited an onset potential of +0.24 V vs. RHE, a maximum FE_{CO}

of 86%, and a partial photocurrent density for CO of −5.52 mA cm^{−2} at −0.8 V vs. RHE, as shown in Figure 4B–D. Additionally, these photocathodes demonstrated superior long-term operational stability for CO production under continuous illumination for 20 h, as shown in Figure 4E. Density functional theory (DFT) calculations indicated that the synergistic effect of Au NPs and TiO₂ enhanced CO₂ adsorption and expedited the generation of the *COOH intermediate and *CO desorption from active sites. This research group further investigated the localized surface plasmon resonance (LSPR) effect of Au on the TiO₂ layer, which contributed to increased activity and selectivity for CO production by utilizing hot electrons generated in Au NPs. Bharath et al. designed photocathodes by integrating plasmonic Ag NPs with TiO₂/RGO (Ag-TiO₂/RGO) via a hydrothermal method followed by microwave irradiation [50]. In this composite, Ag NPs not only absorbed visible light but also acted as efficient electron scavengers, thus enhancing PEC performance for CO₂RR. PEC measurements revealed that the Ag-TiO₂/RGO photocathodes achieved a notable total photocurrent density of 23.5 mA cm^{−2} and exhibited low resistance of 125 Ω in a CO₂-saturated 1.0 M KOH solution under ultraviolet-visible (UV-vis) light illumination. Furthermore, the Ag-TiO₂/RGO photocathodes displayed a CH₃OH yield of 85 μmol L^{−1} cm^{−2}, a QE of 20%, and a faradaic efficiency for CH₃OH (FE_{CH₃OH}) of 60.5% at an onset potential of −0.7 V vs. Ag/AgCl. Bharath et al. also fabricated photocathodes featuring plasmonic-Au and RGO-incorporated α-Fe₂O₃ nanorods (Au/α-Fe₂O₃/RGO) aiming for highly selective CH₃OH production [51]. The synergistic effects among the size-dependent properties of α-Fe₂O₃, the plasmonic nature of Au, and the chemical interactions of Au, RGO, and α-Fe₂O₃ nanorods resulted in a higher band gap for Au/α-Fe₂O₃/RGO (2.60 eV). This band gap allowed the composite to absorb more intensely in the high-energy range of the visible spectrum, enabling the efficient use of photogenerated electrons and reducing e[−]/h⁺ pair recombination effects. Consequently, the Au/α-Fe₂O₃/RGO photocathodes exhibited an impressive photocurrent density of −31.5 mA cm^{−2} and achieved a maximum CH₃OH yield of 43 μmol L^{−1} cm^{−2}, as shown in Figure 4F,G. Additionally, the photocathodes attained QE and FE_{CH₃OH} of 21.5% and 91%, respectively, at −0.6 V vs. SCE in a CO₂-saturated 0.1 M KOH electrolyte under illumination.

Li et al. developed a photocathode for PEC CO₂RR by dispersing Ag NPs onto a Cu-modified mesoporous TS-1 zeolite (Ag/Cu-TS-1) [52]. The fabrication process involved an ion exchange method followed by an in situ photodeposition method, resulting in the synthesis of Cu-TS-1 via ion exchange and the highly dispersed Ag NPs onto Cu-TS-1 through in situ photodeposition. The Ag/Cu-TS-1 photocathode showed exceptional light absorption and efficient separation of e[−]/h⁺ pairs, enhancing CO₂RR. This improvement was attributable to the heterostructure of Cu₂O/CuO and the LSPR effect of the Ag NPs. In PEC performance terms, the Ag/Cu-TS-1 photocathode demonstrated conversion of CO₂ into CH₃OH and C₂H₅OH at rates of 5.64 and 2.62 μmol cm^{−2} h^{−1}, respectively, at −0.6 V vs. RHE in a CO₂-saturated 0.1 M KHCO₃ electrolyte. Zhang et al. constructed a plasmonic Ag-adorned Cu₂O nanowire (Cu₂O/Ag) photocathode for PEC CO₂RR targeting C₂₊ products [53]. The LSPR effect of Ag contributed to both enhanced rapid separation of e[−]/h⁺ pairs and improved surface catalytic reactions for C₂₊ product generation. To substantiate the LSPR effect in the Cu₂O/Ag photocathode,

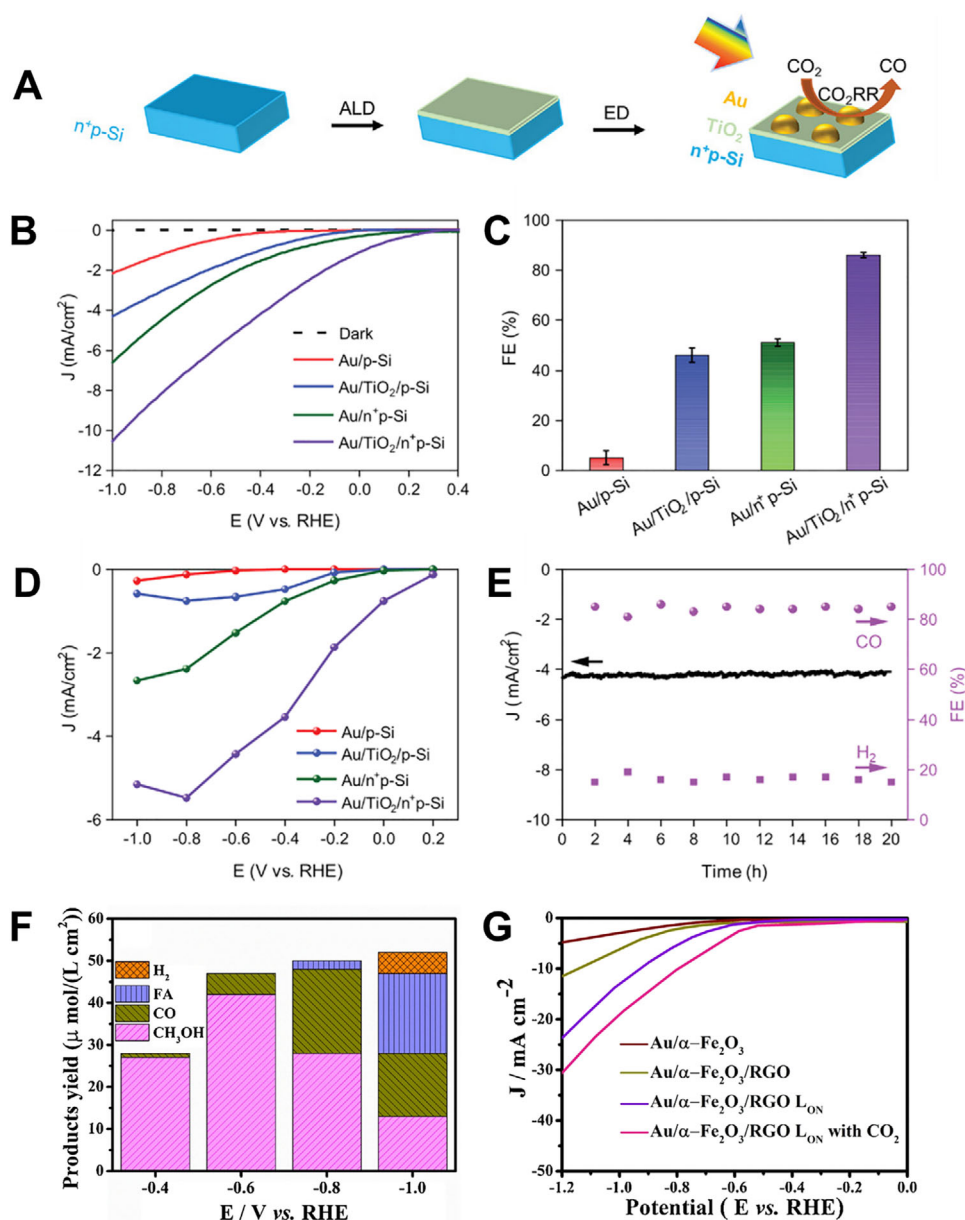


FIGURE 4 | (A) Schematic illustration of the fabrication process of an Au/TiO₂/n⁺p-Si photocathode. (B) LSV curves, (C) FE_{CO}, (D) partial photocurrent density for CO, and (E) long-term operational stability test of the Au/TiO₂/n⁺p-Si photocathode. Reproduced with permission [49]. Copyright 2022, John Wiley and Sons. (F) product yield for the Au/α-Fe₂O₃/RGO photocathode at different potentials (V vs. RHE). (G) total photocurrent density of the Au/α-Fe₂O₃/RGO photocathode. Reproduced with permission [51]. Copyright 2021, Elsevier.

the UV-vis absorption spectrum was used to confirm increased light absorption due to the presence of Ag NPs. Additional in situ attenuated total reflection infrared spectroscopy (ATR-IR) results indicated that incorporating Ag NPs improved the formation and adsorption of the CH₃O* intermediate. PEC tests showed the Cu₂O/Ag photocathode achieved a faradaic efficiency for CH₃COOH (FE_{CH₃COOH}) of 47.7%, with a generation rate of 212.7 μmol cm⁻² h⁻¹ at -0.7 V vs. RHE under illumination.

3.1.2 | Non-Noble Metal

Due to the high structural stability of CO₂ molecules, many semiconductors face challenges in selectively facilitating CO₂RR.

In such scenarios, cocatalysts play a crucial role in minimizing the overpotential required for CO₂RR and enhancing the kinetics to improve overall selectivity. The electrical conductivity of the cocatalyst, along with its adsorption and desorption capabilities based on binding energies with relevant reaction species—especially those with moderate binding affinities for key intermediates—can lead to higher intrinsic CO₂RR activity [54–56]. This, in turn, facilitates the promotion of CO₂RR at lower overpotentials, thereby enhancing onset potentials.

Noble metals, such as Ag and Au, remain efficient catalysts for converting PEC energy into CO₂. However, the use of noble metal-based catalysts faces significant limitations due to their high cost and limited availability, which constrain commercial

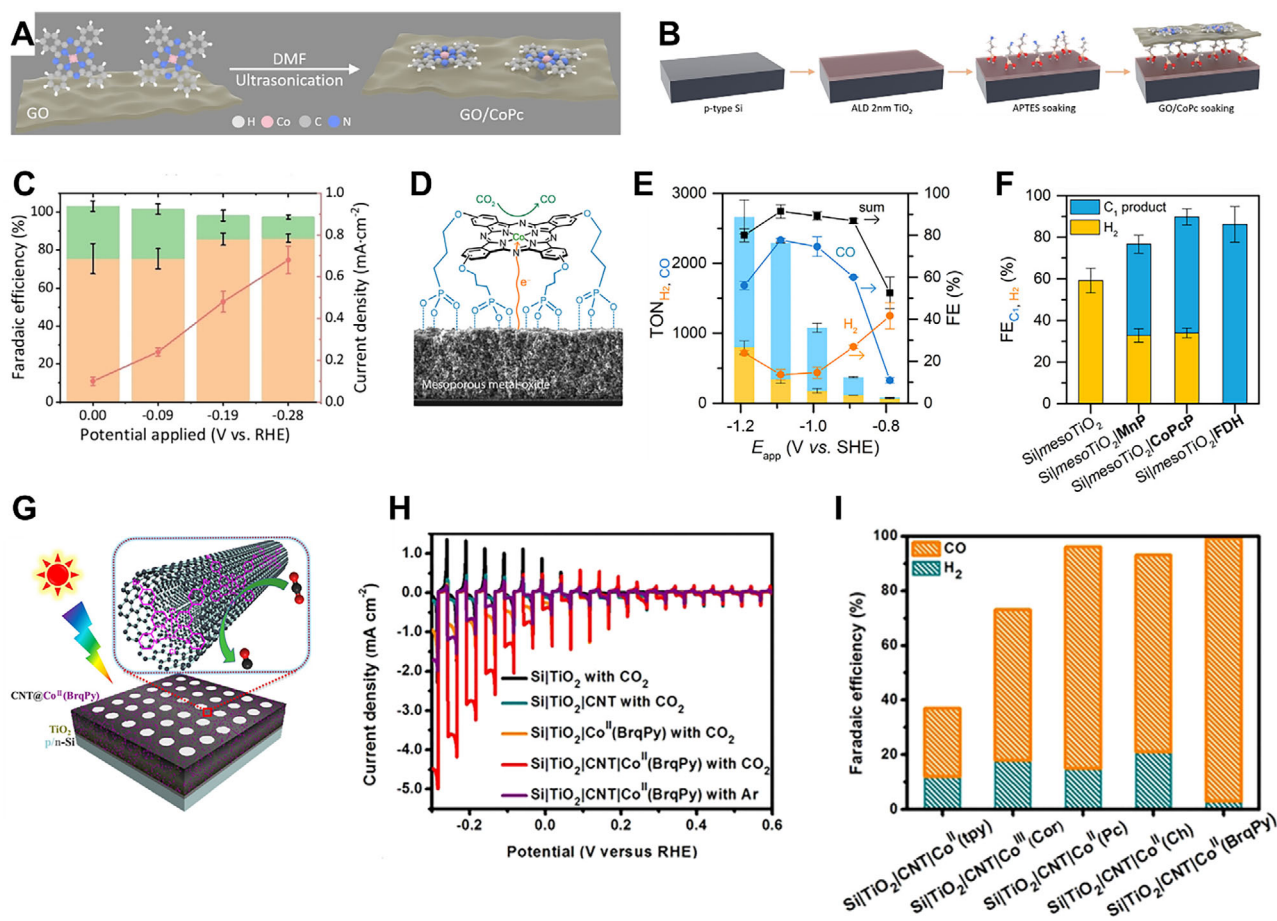


FIGURE 5 | (A) Schematic illustration of the preparation of GO/CoPc and (B) STA-GO/CoPc photocathode. (C) photocurrent density with FE for H₂ and CO of the STA-GO/CoPc photocathode. Reproduced with permission.[62]. Copyright 2022, John Wiley and Sons. (D) Schematic representation of the molecular structure of mesoTiO₂/CoPcP. (E) TON for CO and H₂ of Ti/mesoTiO₂/CoPcP. (F) FE for C₁ and H₂ products yielded by Si/mesoTiO₂/CoPcP and other counterpart photocathodes. Reproduced with permission [63]. Copyright 2021, American Chemical Society. (G) Illustration of the Si/TiO₂/CNT/Co^{II}(BrqPy) photocathode. (H) LSVs and (I) FE for H₂ and CO of the Si/TiO₂/CNT/Co^{II}(BrqPy) photocathode compared with other groups. Reproduced with permission [64]. Copyright 2022, John Wiley and Sons.

implementation [38, 57, 58]. Consequently, extensive research efforts have been directed toward developing alternative catalysts for CO₂RR based on non-noble metal materials, including transition metals. These materials aim to provide low-cost, high-activity, and long-term stability for CO₂RR, addressing the challenges associated with noble metal cocatalysts [38, 59–61].

Among these, cobalt molecular catalysts are widely used as cocatalysts for the photocathode in PEC CO₂RR. For instance, Shang et al. prepared a p-type silicon photocathode incorporating a cobalt phthalocyanine molecular catalyst immobilized on graphene oxide (GO/CoPc) [62]. Initially, CoPc molecules were immobilized on GO through ultrasonication in a DMF solution, taking advantage of GO's conductive properties and capability to facilitate electron transfer, as illustrated in Figure 5A. Subsequently, p-Si wafers, coated with a protective TiO₂ layer (Si-TiO₂), were treated with a solution of (3-aminopropyl)triethoxysilane (APTES), as depicted in Figure 5B. Following this treatment, the Si-TiO₂-APTES (STA) substrate was immersed in a GO/CoPc aqueous dispersion, forming a monolayer-like coating on the surface through electrostatic and hydrogen bonding interactions between the

amine groups of APTES and the carboxylic acid groups of GO. The STA-GO/CoPc achieved a photocurrent density of 0.7 mA cm⁻², while simultaneously attaining a maximum FE_{CO} of 86% at -0.28 V vs. RHE, as observed in Figure 5C. Moreover, STA-GO/CoPc exhibited a remarkably low onset potential of -0.36 V vs. RHE, displaying a FE_{CH₃OH} of 8% at -0.62 V vs. RHE. As shown in Figure 5D, Roy et al. constructed a hybrid photocathode structure comprising a cobalt phthalocyanine catalyst with four phosphonic acid anchoring groups (CoPcP) immobilized on mesoTiO₂, which coated a p-Si photocathode (Si/mesoTiO₂/CoPcP) [63]. Incorporating the four phosphonic acid anchoring groups facilitated the immobilization of the CoPcP catalyst on mesoTiO₂. To assess the impact of the CoPcP catalyst on mesoTiO₂, they synthesized a mesoTiO₂/CoPcP hybrid electrode. As depicted in Figure 5E, the resulting mesoTiO₂/CoPcP photocathode demonstrated highly selective CO₂ to CO conversion, achieving a turnover number for CO (TON_{CO}) of 1949 ± 5 after 2 h of controlled-potential electrolysis at a 550 mV overpotential in a 0.5 M KHCO₃ aqueous electrolyte. In addition, when combined with a p-Si photocathode, the Si/mesoTiO₂/CoPcP exhibited a TON_{CO} of 939 ± 132 with 66% CO selectivity under 0.5 M KHCO₃ conditions, as observed in

Figure 5F. Wen et al. prepared Co^{II} (BrqPy) (BrqPy = 4',4''-bis(4-bromophenyl)-2,2':6',2'':6'',2'''-quaterpyridine) molecular catalysts with multiwalled carbon nanotubes (CNT) on TiO_2 -protected p/n-Si photocathodes ($\text{Si}/\text{TiO}_2/\text{CNT}/\text{Co}^{\text{II}}$ (BrqPy)) [64], as illustrated in Figure 5G. First, a p/n-Si wafer was covered with TiO_2 through atomic-layer deposition (ALD). Then, a CNT layer was drop-cast onto the Si/TiO_2 layer. Finally, a DMF solution containing Co^{II} (BrqPy) molecular catalysts was drop-cast, and the catalysts were immobilized on the CNT layer through π - π stacking interactions. The hybrid photocathodes, benefiting from the highly conductive nature of CNT, achieved a remarkable photocurrent density of up to -1.4 mA cm^{-2} at -0.11 V vs. RHE, as seen in Figure 5H. Furthermore, due to the exceptional activity and selectivity of the cobalt molecular catalyst for CO_2RR , the total FE, and FE_{CO} reached 99% and 97%, respectively, as revealed in Figure 5I. These results surpassed other hybrid photocathodes employing more complex configurations. Leung et al. employed cobalt(II) bis(terpyridine) molecular catalysts (CotpyP) as cocatalysts to construct a highly efficient photocathode for CO_2RR [65]. This hybrid photocathode consisted of a p-type silicon photocathode coated with a mesoporous TiO_2 layer with anchored CotpyP catalysts ($\text{Si}/\text{mesoTiO}_2/\text{CotpyP}$). The mesoporous TiO_2 layer protected the Si, allowing for high loading of CotpyP catalysts and ample surface contact with the electrolyte due to its high surface area. Photoelectrochemical tests indicated CO and HCOO^- production in aqueous acetonitrile (MeCN) with 0.1 M tetrabutylammonium tetrafluoroborate (TBAF_4) and pure CO_2 -saturated 0.1 M KHCO_3 . The turnover number for CO_2RR reached 381 during a 24 h test in aqueous MeCN. Furthermore, nanowires (NWs), NPs, metal oxides, and MOFs, which consist of non-noble metals, are also widely used as photocathodes in PEC CO_2RR . For example, Dong et al. designed a photocathode comprising CuS-covered GaN NWs on silicon wafers ($\text{CuS}/\text{GaN}/\text{Si}$) to convert H_2S -containing CO_2 mixture gas to HCOOH efficiently [66]. The fabrication involved thermally evaporating Cu NPs and plasma-assisted molecular beam epitaxy (MBE) of GaN NWs on Si wafers. PEC experiments were conducted in a 0.1 M KHCO_3 solution purged with CO_2 and H_2S mixture gas under 1-sun illumination, as shown in Figure 6A. Notably, Cu NPs spontaneously transformed into CuS NPs during the PEC experiment. Compared to other photocathodes of Cu/Si, CuS/Si, and Cu/GaN/Si, the CuS/GaN/Si photocathode revealed an outperforming faradaic efficiency for HCOOH (FE_{HCOOH}) of 70.2% at -1.0 V vs. RHE and achieved a maximum current density for HCOOH of 7.07 mA cm^{-2} , as shown in Figure 6B,C. Dong et al. fabricated Bi NP cocatalysts supported on GaN NWs photocathodes for PEC CO_2RR to HCOOH [67]. Focusing on the electronic interaction between Bi NPs and GaN NWs grown on a planar Si wafer ($\text{Bi}/\text{GaN}/\text{Si}$), the strong electronic interaction enhanced CO_2 conversion due to electron sharing between Bi NPs and GaN NWs. The Bi/GaN/Si photocathode demonstrated outstanding selectivity for HCOOH , achieving a FE_{HCOOH} of $\sim 98\%$ at -0.3 V vs. RHE, a high current density of 10.3 mA cm^{-2} at -0.6 V vs. RHE, and sustained stable operation for 12 h under 1-sun illumination. This underlines the critical role of electronic interactions between photocathodes and cocatalysts in enhancing PEC performance. Zhou et al. showcased a novel nanoarchitecture with a Sn NP/GaN NW/Si photocathode for aqueous PEC reduction of CO_2 to HCOOH [68]. Integrating defect-free GaN NWs grown on a planar Si via MBE with electrodeposited Sn NPs, the photocathode's PEC

testing revealed exceptional performance, unprecedented TOF of 107 min^{-1} , a total current density of 17.5 mA cm^{-2} , and a high FE_{HCOOH} of 76.9% at a low potential of -0.53 V vs. RHE under 1-sun illumination, corresponding to a productivity of $201 \mu\text{mol cm}^{-2} \text{ h}^{-1}$. The photocathode also exhibited a high TON for HCOOH production, reaching 64,000 during stable operation over 10 h. DFT calculations suggested that the synergistic effects of covalent Ga-C bonding and ionic-like Sn-O bonding played a crucial role in activating CO_2 , contributing to the remarkable activity and selectivity for CO_2RR . As presented in Figure 6D, Deng et al. developed a Cu_2O photocathode coated with MOFs named $\text{Cu}_3(\text{BTC})_2$ (BTC = benzene-1,3,5-tricarboxylate) for PEC CO_2RR to CO [69]. The $\text{Cu}_3(\text{BTC})_2$ coating played multiple roles in the PEC CO_2RR process, including preventing photocorrosion of the Cu_2O layer, facilitating electron transfer, and providing catalytic active sites for CO_2RR . PEC performance was measured in a CO_2 -saturated MeCN containing 0.1 M tetrabutylammonium hexafluorophosphate (TBAF_6). Results indicated that the $\text{Cu}_3(\text{BTC})_2/\text{Cu}_2\text{O}/\text{ITO}$ photocathode reached a maximum FE_{CO} of about 95% at applied potentials ranging from -1.77 to -1.97 V vs. ferrocene/ferrocenium (Fc/Fc^+), as displayed in Figure 6E. Furthermore, the solar-to-CO (STC) efficiency of this photocathode reached 0.83% at -2.07 V vs. Fc/Fc^+ under AM 1.5G illumination, as observed in Figure 6F. Long-term chronoamperometry indicated that the photocathode maintained a nearly constant current density under visible light and a steady photocurrent density under chopped visible light, highlighting its stability and performance under varying light conditions.

As illustrated in Figure 6G, Wang et al. constructed a hybrid photocathode structure comprising CuO adorned with asymmetric Cu-N sites (CuN_x/CuO) for PEC CO_2RR [70]. The CuN_x/CuO photocathode exhibited a faradaic efficiency towards C_2 products (FE_{C_2}) of 15.2%, accompanied by a photocurrent density of -1.0 mA cm^{-2} at 0.2 V vs. RHE in CO_2 -saturated 0.1 M KHCO_3 under AM 1.5G simulated sunlight. DFT calculations demonstrated that the adsorption of OCCO^* and $^*\text{COCH}_2$ intermediates on Cu-N sites, crucial for the formation of C_2 products, was more favorable than on Cu-Cu sites, as presented in Figure 6H,I. Theoretical calculations also indicated that the CuN_x/CuO photocathode had higher electron migration efficiency than CuO due to the asymmetric d-p orbitals at Cu-N sites, which lowered the energy barrier for C-C coupling. Roh et al. fabricated Si NWs connected with a Cu NP ensemble to create photocathodes (Cu NPs/Si NWs) for PEC CO_2RR to C_2H_4 [71]. Assessed under 100 mW cm^{-2} air mass (AM) 1.5 simulated sunlight in CO_2 -purged 0.1 M KHCO_3 , the photocathode achieved a selectivity for CO_2RR to C_2H_4 with a faradaic efficiency ($\text{FE}_{\text{C}_2\text{H}_4}$) of approximately 25% and demonstrated activity with partial current densities exceeding 2.5 mA cm^{-2} at -0.50 V vs. RHE. Moreover, the Cu NPs/Si NWs photocathode exhibited long-term stability, maintaining PEC CO_2RR under 50 h of continuous bias and illumination. Kim et al. constructed a metal-insulator-semiconductor (MIS) structure comprising $\text{Cu}/\text{TiO}_2/\text{p-Si}$ photocathodes for PEC CO_2RR to multicarbon products [72]. They also investigated the effects of ionomer bilayer coatings, specifically Nafion atop Sustainion, on the Cu surface of the $\text{Cu}/\text{TiO}_2/\text{p-Si}$ MIS photocathodes. PEC testing indicated that $\text{Cu}/\text{TiO}_2/\text{p-Si}$ photocathodes coated with Nafion on top of Sustainion revealed partial current densities for C_2H_4 ranging from -0.9 mA cm^{-2} to -2.3 mA cm^{-2} in CO_2 -saturated 0.1 M $\text{C}_2\text{H}_5\text{CO}_3$ under wet-side illumination, compared

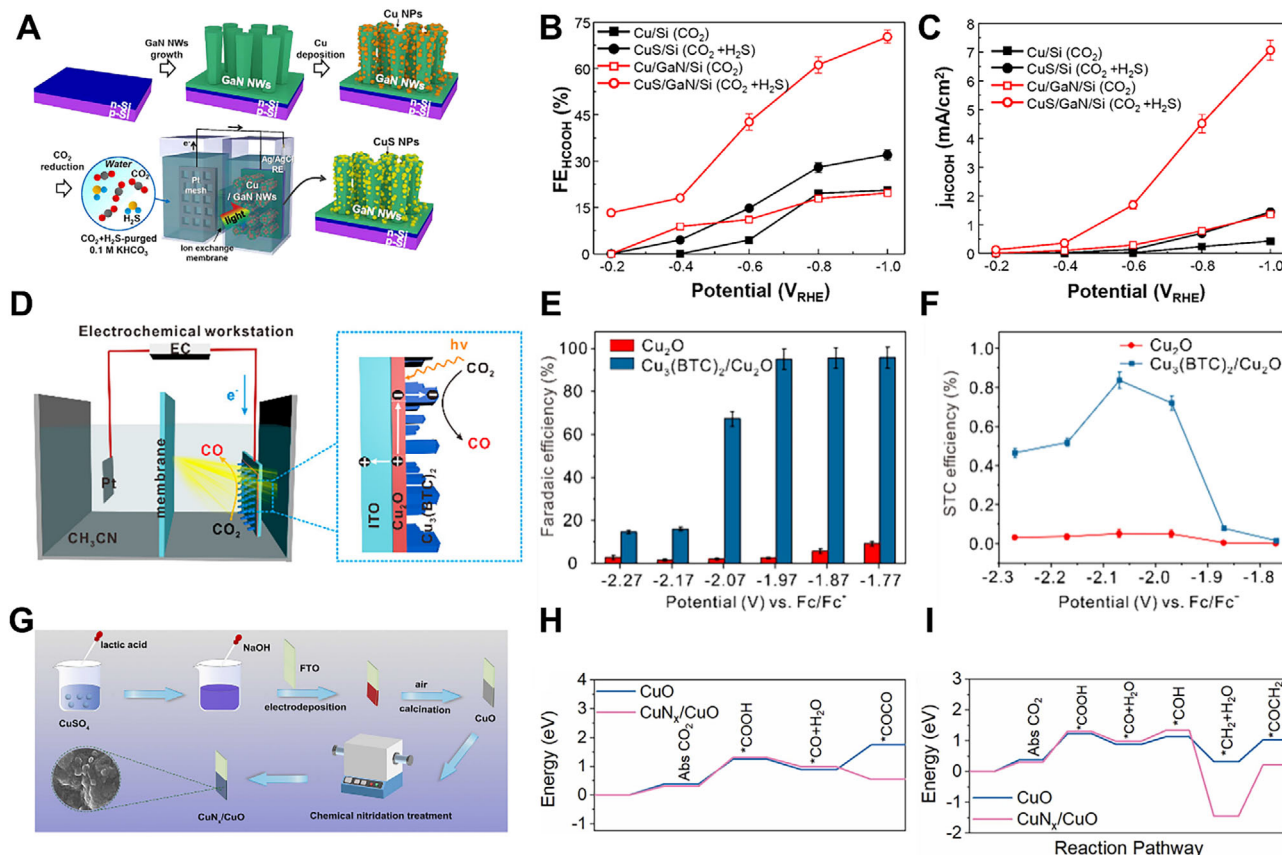


FIGURE 6 | (A) Schematic illustration of the CuS/GaN/Si photocathode synthesis and PEC experiments. (B) FE_{HCOOH} and (C) j_{HCOOH} of the CuS/GaN/Si photocathode. Reproduced with permission [66]. Copyright 2021, American Chemical Society. (D) Schematic depiction of the PEC experiments of Cu₃(BTC)₂/Cu₂O photocathode. (E) FE_{CO} and (F) STC efficiency of the Cu₂O and Cu₃(BTC)₂/Cu₂O/ITO photocathode. Reproduced with permission [69]. Copyright 2019, American Chemical Society. (G) Schematic illustration of the Cu_{Nx}/CuO photocathode synthesis. The calculated energy barrier for forming (H) EtOH and (I) acetate for the CuO and Cu_{Nx}/CuO photocathode. Reproduced with permission [70]. Copyright 2022, Elsevier.

to the condition without ionomer bilayers on the Cu surface. This underscores the enhancement of both activity and selectivity for C₂H₄ due to the Cu cocatalyst and bilayer coatings.

3.2 | Junction Engineering

A heterojunction is typically defined as a structure composed of two or more different semiconductors with a contacting interface, distinct band energy levels, a matching crystal lattice, and similar thermal expansion coefficients [73]. Heterojunctions can be classified into type-I, type-II (including p-n junctions), and Schottky barrier junctions (metal-semiconductor). Semiconductor heterojunctions often involve interfacing two semiconductor materials with differing Fermi-level energies, creating a built-in electric field that promotes the separation of electrons and holes upon light excitation.

In the case of type-I heterojunctions, two semiconductors with overlapping band structures typically exhibit one semiconductor with a more negative CB position and a more positive VB position than the other semiconductor. Conversely, in type-II heterojunctions, the two semiconductors have staggered band structures where electrons transition from a more negative CB to

a less negative CB, and holes move in the opposite direction. In type-II heterojunctions, photogenerated electrons and holes are efficiently separated, allowing for e⁻/h⁺ pairs to be excited using a greater number of photons [73].

Schottky barrier junctions create band bending near the semiconductor-metal catalyst interface, facilitating electron transfer from the semiconductor to the metal. Nevertheless, this section focused solely on semiconductor heterojunctions, as Schottky barrier junctions overlap with concepts such as cocatalysts, and there is extensive prior research in this domain.

For example, Quyang et al. prepared a photocathode tailored for PEC CO₂RR to HCOOH, consisting of Bi-modified 1D ZnO/α-Fe₂O₃ nanotubes (1D Bi@ZFO NTs) [74]. The formation of an n-n heterojunction between the narrow bandgap of α-Fe₂O₃ and the wide bandgap of ZnO was instrumental in enhancing charge transfer, establishing an internal electric field conducive to driving the transfer of photoexcited charges, as illustrated in Figure 7A. Additionally, depositing Bi onto the ZnO/α-Fe₂O₃ heterojunction potentially increased the carrier concentration at the electrode surface, thereby enhancing the efficiency of photogenerated charge separation. Consequently, the Bi@ZFO NTs photocathode indicated a low onset potential of

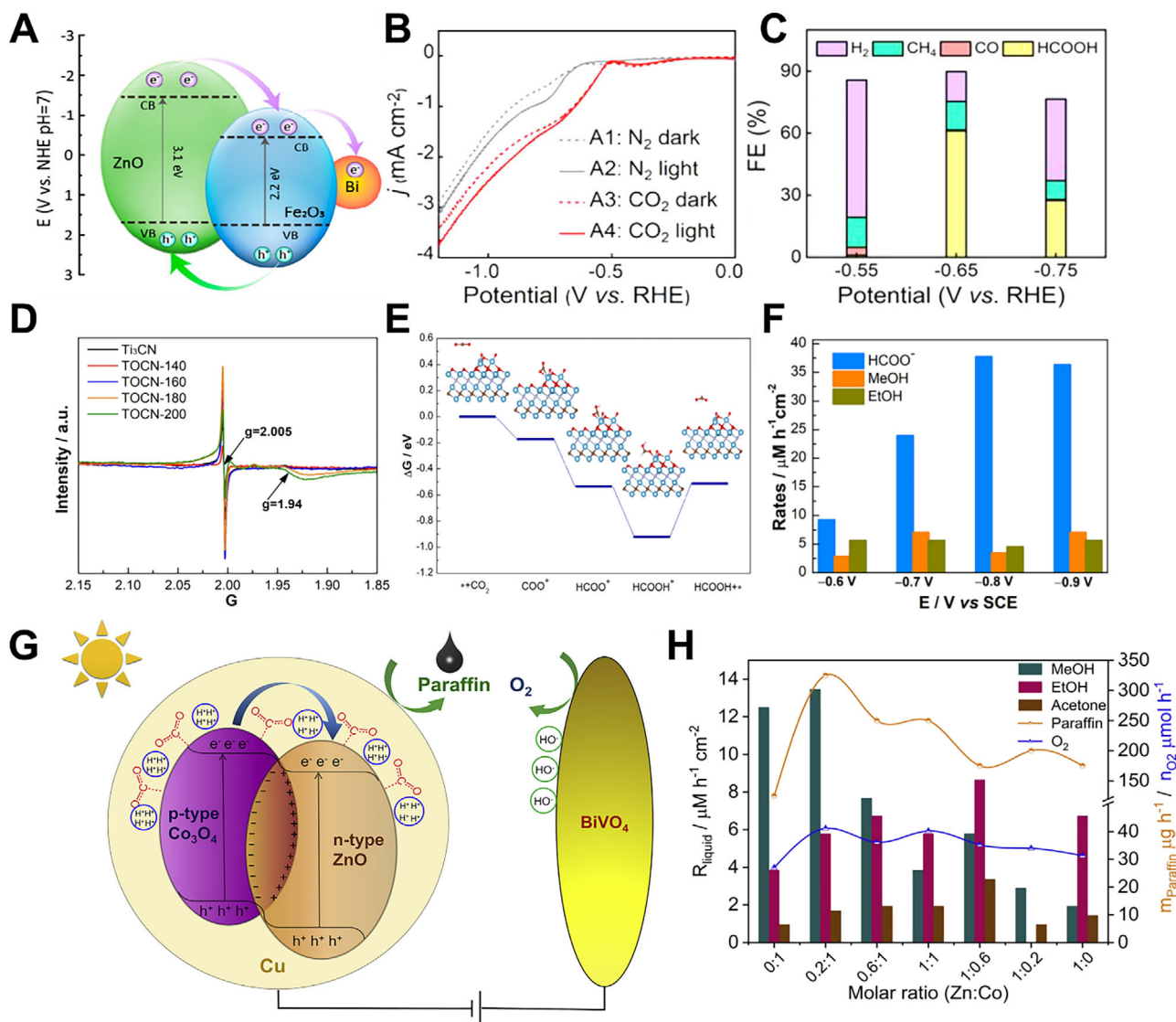


FIGURE 7 | (A) Proposed PEC CO₂RR mechanism of 1D Bi@ZFO NTs photocathode. (B) LSV curves and (C) FE of H₂, CH₄, CO, and HCOOH of the 1D Bi@ZFO NTs photocathode. Reproduced with permission [74]. Copyright 2022, American Chemical Society. (D) EPR spectra and (E) calculated Gibbs free energy of forming HCOOH. (F) Various product yield rates of the TiO₂/Ti₃CN MXene photocathode. Reproduced with permission [79]. Copyright 2023, Elsevier. (G) Proposed mechanism of PEC CO₂RR to paraffin products and (H) paraffin yield rate of Zn_x-Co_y@Cu photocathode. Reproduced with permission [84]. Copyright 2020, Elsevier.

−0.53 V vs. RHE, a low Tafel slope of 101.2 mV dec^{−1}, and achieved a high FE_{HCOOH} of 61.2% at −0.65 V vs. RHE, maintaining stability over 4 h under visible light, as shown in Figure 7B,C. Jiang et al. reported a photocathode incorporating CuO onto graphitic carbon nitride (g-C₃N₄) supported on carbon paper (CuO/g-C₃N₄/carbon paper) for PEC CO₂RR to CH₃OH [75]. Establishing a type-I heterojunction facilitated photogenerated electron transfer from the CB of g-C₃N₄ to the CB of CuO, which has a relatively less negative CB energy level under illumination. Concurrently, favorable hole transfer occurred from the VB of g-C₃N₄ to the VB of CuO, which held a lower VB energy. As a result, the CuO/g-C₃N₄/carbon paper photocathode exhibited a high IPCE, an increased photocurrent response, and a remarkable FE of 75% and QE of 8.9%, respectively, for CH₃OH production. Pan et al. presented a photocathode consisting of a Cu catalyst decorated with flower-like CeO₂ NPs and CuO NPs, functioning as n-type and p-type semiconductors, respectively [76]. The

formation of a p-n heterojunction with CeO₂ NPs/CuO NPs facilitated the synergistic migration of photoexcited electrons and holes, leading to exceptional PEC performance for CO₂RR. Thus, the CeO₂ NPs/CuO NPs/Cu photocathode revealed a CH₃OH yield rate of 3.44 $\mu\text{mol cm}^{-2} \text{h}^{-1}$ and exhibited a high FE_{CH₃OH} of approximately 60% at −1.0 V vs. saturated calomel electrode (SCE) under visible light irradiation. Zheng et al. utilized zinc phthalocyanine (ZnPc) integrated with carbon nitride nanosheets as a photocathode for PEC CO₂RR to CH₃OH [77]. The aligned energy bands between ZnPc and carbon nitride facilitated electron transfer and reduced recombination of the e[−]/h⁺ pair. Simultaneous exposure to light and an external voltage ensured that reductive electrons were generated not only through light excitation but also by the external voltage. This augmented the transfer rate of photogenerated electrons from the CB of carbon nitride to the LUMO of ZnPc. Consequently, the ZnPc/carbon nitride photocathode exhibited a predominant CH₃OH product with a yield of

13 $\mu\text{mol L}^{-1}$ after 8 h at -1.0 V vs. SCE. Tarek et al. developed a heterostructured $\text{CdS}-\text{CuFe}_2\text{O}_4$ photocathode to convert CO_2 into CH_3OH [78]. The $\text{CdS}-\text{CuFe}_2\text{O}_4$ photocathode exhibited a higher IPCE of 12.09% compared to CuFe_2O_4 with an IPCE of 7.28% at 470 nm, illustrating effective visible light absorption during PEC CO_2RR . Within the $\text{CdS}-\text{CuFe}_2\text{O}_4$ heterojunction, the CB of CdS served as the site for CO_2RR , capturing photogenerated electrons originating from CuFe_2O_4 , while water oxidation occurred at the VB of CuFe_2O_4 . Accordingly, PEC performance indicated that the $\text{CdS}-\text{CuFe}_2\text{O}_4$ photocathode revealed an $\text{FE}_{\text{CH}_3\text{OH}}$ of 72% and a $\text{QE}_{\text{CH}_3\text{OH}}$ of 16.9% and recorded a maximum CH_3OH yield of 23.8 $\mu\text{mol L}^{-1} \text{ cm}^{-2}$ in CO_2 -saturated 0.1 M NaHCO_3 electrolyte. Xu et al. prepared a 2D heterojunction of $\text{TiO}_2/\text{Ti}_3\text{CN}$ MXene as a photocathode for PEC CO_2RR , synthesized using a simple hydrothermal oxidation method [79]. The 2D $\text{TiO}_2/\text{Ti}_3\text{CN}$ heterojunction, with its large specific surface area, exceptional light absorption ability, and abundant Ti^{3+} species, facilitated the efficient generation and migration of e^-/h^+ pairs. To confirm the impact of Ti^{3+} , electron paramagnetic resonance (EPR) spectra were obtained, as depicted in Figure 7D. The EPR spectra demonstrated widespread detection of Ti^{3+} species, proving beneficial for trapping charge carriers and mitigating the recombination of e^-/h^+ pairs. Furthermore, DFT calculations suggested that the 2D $\text{TiO}_2/\text{Ti}_3\text{CN}$ heterojunction could spontaneously adsorb CO_2 molecules and stabilize key intermediates crucial for HCOOH production, as shown in Figure 7E. Consequently, the novel PEC system, composed of $\text{Pd}@\text{TiO}_2/\text{Ti}_3\text{CN}||\text{SCE}||\text{BiVO}_4$, effectively produced HCOO^- , CH_3OH , and $\text{C}_2\text{H}_5\text{OH}$ with a remarkable formation rate of 45.6 $\mu\text{M cm}^{-2} \text{ h}^{-1}$, as depicted in Figure 7F. Lu et al. developed a photocathode for PEC CO_2RR to $\text{C}_2\text{H}_5\text{OH}$, comprising arrays of 0D/1D $\text{CuFeO}_2/\text{CuO}$ nanowire heterojunction arrays synthesized through an in situ method [80]. Due to the comparable energy band gaps of CuO and CuFeO_2 , the photogenerated electrons originating from the CB of CuFeO_2 migrated to the surface of CuO , while photogenerated holes derived from the VB of CuO moved to CuFeO_2 . This arrangement suppressed the recombination of e^-/h^+ pairs under the built-in electric field of the heterojunction. The PEC performance of the $\text{CuFeO}_2/\text{CuO}$ nanowire photocathode exhibited an impressive faradaic efficiency for $\text{C}_2\text{H}_5\text{OH}$ ($\text{FE}_{\text{C}_2\text{H}_5\text{OH}}$) of 66.73% at -0.6 V vs. Ag/AgCl . Zhang et al. designed a $\text{CuFeO}_2/\text{TNNTs}$ photocathode, incorporating high-temperature-durable n-type Nb-doped TiO_2 nanotube arrays (TNNTs) and p-type CuFeO_2 for PEC CO_2RR [81]. Initially, TNNTs were synthesized through anodic oxidation on TiNb alloy sheets. Subsequently, $\text{CuFeO}_2/\text{TNNTs}$ were constructed by coating precursor solution on TNNTs, followed by annealing in an argon atmosphere. The high heat stability of TNNTs preserved the well-maintained structure of regular nanotube arrays. Additionally, TNNTs exhibited semiconductor properties comparable to those of n-type TiO_2 , enabling their integration with p-type CuFeO_2 to form a p-n heterojunction. As a result, the $\text{CuFeO}_2/\text{TNNTs}$ photocathode exhibited high light absorption and accelerated carrier transport due to a suitable band gap and the presence of the p-n heterojunction. In addition, the $\text{CuFeO}_2/\text{TNNTs}$ photocathode demonstrated an outstanding photocurrent of 80 $\mu\text{A cm}^{-2}$, resulting in $\text{C}_2\text{H}_5\text{OH}$ production at a rate of 3.3 $\mu\text{mol}/5\text{h}\cdot\text{cm}^{-2}$. Wang et al. presented a photocathode, designated as BCW-X, which was achieved by depositing a $\text{Bi}_2\text{WO}_6/\text{BiOCl}$ heterojunction onto an F- SnO_2 substrate through an in situ hydrothermal process [82]. Notably, the exposed pristine (101) crystal plane of BiOCl transformed into

the (112) plane in the heterojunction, facilitated by the excellent compatibility between the (112) planes of BiOCl and the (113) planes of Bi_2WO_6 . Simultaneously, the heterojunctions in BCW-X maintained a 2D layered structure, thereby enhancing the efficiency of e^-/h^+ pair separation. PEC experiments were conducted in a $\text{BCW-6}(\text{KHCO}_3)|\text{BiVO}_4$ PEC cell under illumination from an Xe lamp, with an external voltage ranging from -0.6 to 1.1 V. The $\text{BCW-6}(\text{KHCO}_3)|\text{BiVO}_4$ system achieved a $\text{C}_2\text{H}_5\text{OH}$ yield rate of 600 $\mu\text{mol h}^{-1} \text{ g}^{-1}$ with an exceptional selectivity of 80% at -1.0 V.

Wang et al. reported, for the first time, a g- $\text{C}_3\text{N}_4/\text{ZnTe}$ type-II heterojunction photocathode for PEC CO_2RR to $\text{C}_2\text{H}_5\text{OH}$ [83]. This heterojunction facilitated the efficient separation of photoexcited e^-/h^+ pairs and promoted electron transfer from ZnTe to g- C_3N_4 , driven by the establishment of an interfacial internal electric field (IEF) created between the two semiconductors. The g- $\text{C}_3\text{N}_4/\text{ZnTe}$ photocathode displayed a remarkable $\text{C}_2\text{H}_5\text{OH}$ production rate of 17.1 $\mu\text{mol cm}^{-2} \text{ h}^{-1}$ at -1.1 V vs. Ag/AgCl . Furthermore, DFT calculations suggested that the collaboration between ZnTe, with high CO_2 adsorption ability, and g- C_3N_4 , rich in pyridinic N, played a role as a CO-producing site, achieving the C-C coupling process through the adsorption of CO with proton-coupled electron transfer. Wang et al. utilized 3D C/N-doped heterojunctions of $\text{Zn}_x\text{Co}_y@\text{Cu}$ as a photocathode for PEC CO_2RR to paraffin products [84]. The $\text{Zn}_x\text{Co}_y@\text{Cu}$ photocathode consisted of p-type semiconductor Co_3O_4 and n-type semiconductor ZnO on Cu foam, forming heterojunctions with various active sites that led to outstanding C-C coupling for paraffin product generation. Upon exposure to light irradiation in a PEC cell, the $\text{Zn}_x\text{Co}_y@\text{Cu}$ photocathode generated photoexcited e^-/h^+ pairs, which were rapidly separated by the built-in electric field, leading to enhanced mobilities of charge carriers, as illustrated in Figure 7G. Electrons could migrate from the CB of p-type Co_3O_4 to the CB of n-type ZnO, while holes were either trapped by electrons from the PEC cell circuit or reacted with OH. Therefore, the high concentration of photoelectrons was captured by protons on the surface, resulting in the formation of abundant active hydrogen atoms capable of converting multiple CO_2 molecules into paraffin products. The $\text{Zn}_x\text{Co}_y@\text{Cu}$ photocathode demonstrated its optimal PEC performance by achieving a paraffin yield rate of 325 $\mu\text{g h}^{-1}$ at -0.4 V vs. SCE, all while avoiding the release of H_2 , as observed in Figure 7H.

3.3 | Nanostructure Engineering

Nanostructure engineering is an effective method for enhancing the performance of photocathodes by manipulating the dimensions and morphology of photocathode materials at the nanometer scale [85, 86]. Notable examples of these nanostructures include nanorods, nanowires, dendritic structures, core/shell structures, as well as highly nanoporous and hollow structures. The benefits of employing such nanostructures are manifold. They facilitate enhanced light absorption through scattering and reduce bulk recombination. Additionally, these structures increase the specific surface area, leading to a corresponding increase in active sites [87].

Furthermore, nanostructure engineering involves tuning the crystallographic orientations. Semiconductor nanocrystals

typically exhibit anisotropic characteristics, composed of face-dependent electronic structures, adsorption energy/reactive sites, and photocorrosion resistance, attributable to different atomic configurations and coordination on various crystal facets [88–93]. Overall, synthesizing nanostructures with a high aspect ratio improves light harvesting and charge separation in the semiconductor bulk [55]. Additionally, nanostructures that expose selective facets, favorable for CO₂RR kinetics, enhance charge separation at the surface.

For example, Liu et al. fabricated a photocathode for PEC CO₂RR to CO by combining InP nanopillar arrays with Au-TiO₂ interfaces (Au-TiO₂/InP) [94]. In the fabrication process, they used inductively coupled plasma reactive ion etching (ICP-RIE) on Au/SiO_x-masked InP wafers to synthesize InP NPs. However, ICP-RIE led to plasma-induced surface defects on the InP NPs, resulting in a reduced minority carrier lifetime compared to planar InP. To remedy this, a dilute HCl solution was used to remove the plasma-damaged layer, leading to fewer surface defects in the InP NPs and improved minority carrier lifetime, as shown in Figure 8A. Thus, these treatments, aimed at eliminating surface defects, contributed to an increased surface area, reduced light reflection, and minimized carrier recombination losses, ultimately enhancing light-harvesting efficiency. The PEC performance of the nanostructured Au-TiO₂/InP photocathodes demonstrated an onset potential of +0.3 V vs. RHE and an FE_{CO} of 84.2% at −0.11 V vs. RHE in a CO₂-purged 0.1 M KHCO₃ solution under simulated 1 sun illumination, as illustrated in Figure 8B,C. Hu et al. developed a photocathode for PEC CO₂ conversion into CO featuring uniformly dispersed Au NPs with Au (111)/Au (200) boundaries on the p-Si surface (b-Au₁/Si) [95]. Initially, small, consistently sized Au seeds were distributed on the p-Si surface using a chemical deposition (CD) method. Subsequent electrodeposition ensured continuous growth of the Au above the CD seeds, maintaining a homogeneous distribution, as depicted in Figure 8D. DFT calculations suggested that the presence of Au (111)/Au (200) boundaries substantially decreased the energy barrier for forming the *COOH intermediate during CO₂RR. As a result, the b-Au₁/Si photocathode achieved an impressive photocurrent density of −13.1 mA cm^{−2} at −1.0 V vs. RHE with an FE_{CO} of 82.2% at −0.4 V vs. RHE, and it maintained remarkable operational stability for over a week, as shown in Figure 8E,F. Mubarak et al. prepared a 3D nanoporous structured TiO₂ NPs on a thin Ti foil photocathode for CO₂RR to HCOOH; the process involved a chemical treatment with H₂O₂, followed by calcination at elevated temperatures ranging from 400 to 800°C [96]. The resulting 300 to 500 nm thick 3D nanoporous layer on the Ti-foil surface displayed significant porosity. This structure enhanced the photon conversion efficiency of TiO₂ NPs, increasing photon absorption per unit surface area and strengthening the electrochemical reaction capabilities due to the large specific surface area. The photocathode produced HCOOH as the primary product in PEC CO₂RR after more than 25 h of chronoamperometric electrolysis and achieved an FE_{HCOOH} of 64% with an HCOOH yield of 165 μmol cm^{−2} h^{−1} at −1.3 V vs. Ag/AgCl. Paul et al. designed a photocathode using a morphology-controlled synthesis of Ag NPs distributed onto WO₃ nanorods (Ag/WO₃-NR) for PEC CO₂RR to HCOO[−] [97]. The one-pot fabrication process employed cetyltrimethylammonium bromide (CTAB) as a structure-directing agent for forming WO₃ nanorods. Critical parameters such as CTAB concentration,

reflux time, and temperature were pivotal in determining the nanorod morphology. The Ag/WO₃-NR photocathode exhibited a significant current density of 0.4 mA cm^{−2} for HCOO[−] production and achieved a rate of 31.7 mmol h^{−1}.

Gurudayal et al. constructed a photocathode for PEC CO₂RR to C₂₊ products, utilizing a back-illuminated n-type Si absorber covered with an Ag-supported dendritic Cu catalyst [98]. The synthesis of the Ag-supported dendritic Cu catalyst involved the evaporation of Ag, followed by high-rate electrodeposition of Cu, resulting in a highly porous structure with nanocactus-like morphology and featuring a dendritic Cu structure on the pyramid-shaped Ag. The Ag-supported dendritic Cu catalyst exhibited a high electrochemically active surface area, enabling the photocathode to operate at a high current density. Therefore, the photocathode produced C₂₊ products, including C₂H₄, C₂H₅OH, and C₃H₇OH, in CO₂-saturated 0.1 M CsHCO₃ under simulated one sun illumination. Additionally, the photocathode maintained over 60% FE for hydrocarbon and oxygenated products, primarily C₂H₄, C₂H₅OH, and C₃H₇OH, for several days under simulated diurnal illumination. Kempler et al. utilized high loadings of Cu integrated onto Si microwire arrays (n⁺p-Si μW/Cu) for PEC CO₂RR to C₂H₄ [99]. The Si microwire array structure could diminish trade-offs between catalyst loading and light absorption intensity. A Si photocathode with Cu electrodeposited onto the vertical sidewalls of high-aspect-ratio microwires was designed to minimize parasitic absorption by the catalyst, as revealed in Figure 8G, demonstrating a |J_{ph}| exceeding 25 mA cm^{−2} before and after 48 h of PEC CO₂RR, resulting in the production of C₂H₄ at more positive potentials under 1-sun illumination. Thus, the n⁺p-Si μW/Cu photocathode revealed a maximum |J_{C₂H₄}| of 2.1 ± 0.2 mA cm^{−2} at −0.44 V vs. RHE and a maximum |J_{CH₄}| of 2.9 ± 0.7 mA cm^{−2} at −0.62 V vs. RHE, as shown in Figure 8H,I.

3.4 | Defect Engineering

Defect engineering, beyond doping, involves native point defects such as vacancies and interstitials occurring naturally during material synthesis, influencing catalytic, electrical, and optical properties. These defects are now recognized as a strategy to enhance photoactivity in photoelectrode. Classified based on dimensional space, defects include 0D (point defects), 1D (line defects), 2D (interface defects), and 3D (bulk defects) [100–104]. Their roles encompass both geometric and electronic effects, acting as adsorption sites due to their high energy state and influencing electronic structures. Defects, with their dynamic structures, improve activation and diffusion in stable CO₂ reactions. Additionally, they alter electronic structures to affect adsorption energy, steering reaction pathways in processes like CO₂RR. The controlled fabrication of desirable defects is crucial for successful defect engineering, enhancing CO₂RR kinetics, and minimizing catalysis-recombination trade-offs without needing external catalytic entities [105–109].

As shown in Figure 9A,B, Dong et al. investigated grain boundary (GB) oxidation in Cu–Ag thin films and its impact on the selectivity of CO and CH₄ production [110]. They developed a photocathode incorporating a Cu–Ag thin-film cocatalyst and p-type Si to enhance the efficiency of PEC CO₂RR, as revealed

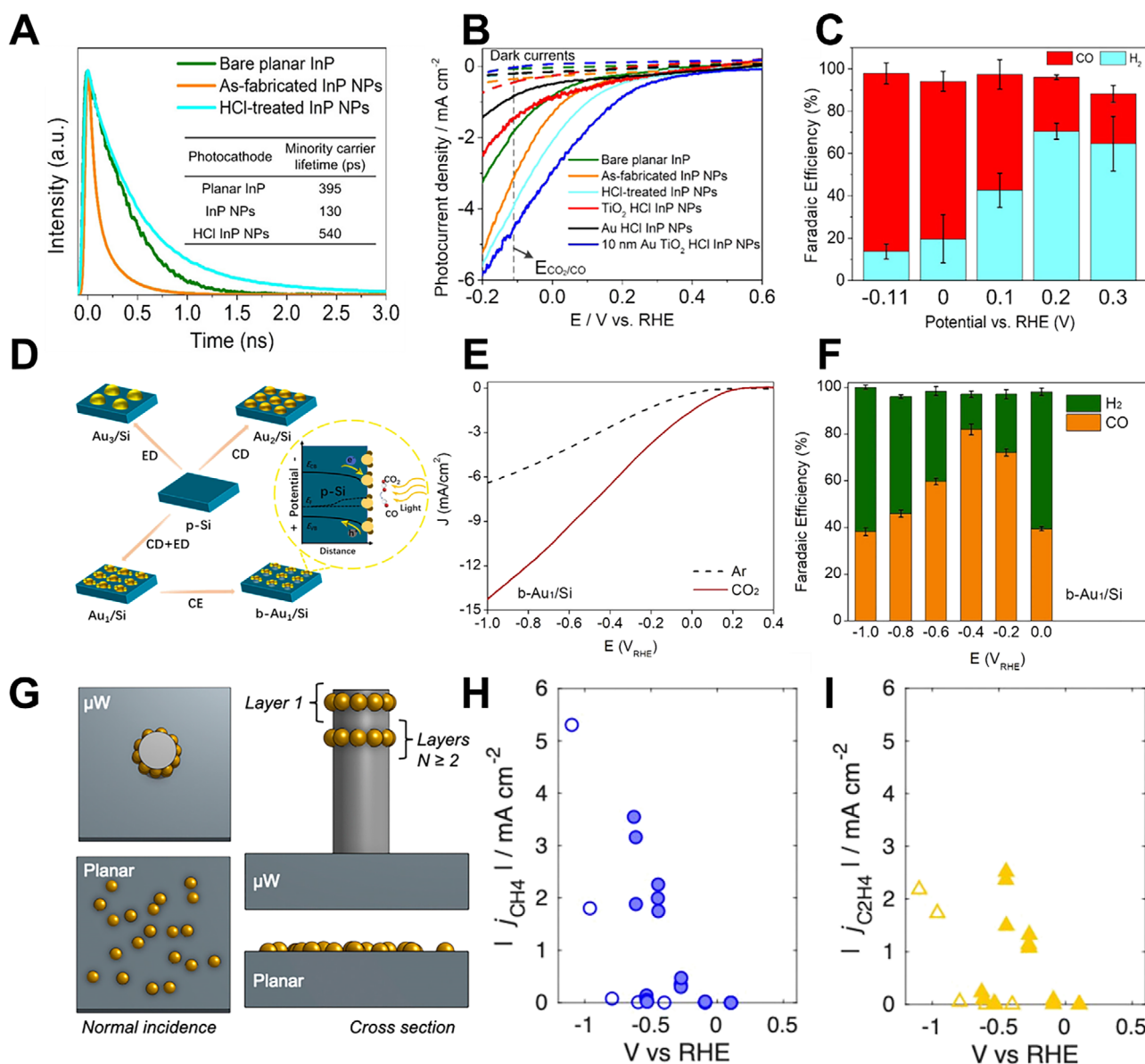


FIGURE 8 | (A) TRPL spectra of samples. (B) Photocurrent density and (C) FE_{CO} and FE_{H_2} of the Au-TiO₂/InP photocathode. Reproduced with permission [94]. Copyright 2021, American Chemical Society. (D) Schematic of the fabrication process, (E) LSV curves, and (F) FE_{CO} and FE_{H_2} of the b-Au₁/Si photocathode. Reproduced with permission [95]. Copyright 2023, Elsevier. (G) Schematic illustration of the n⁺p-Si μW/Cu photocathode. (H) j_{CH_4} and (I) $j_{C_2H_4}$ of the n⁺p-Si μW/Cu photocathode. Reproduced with permission [99]. Copyright 2020, American Chemical Society.

in Figure 9C. The electron beam evaporation method facilitated the direct growth of Cu thin films on the substrate, with the grain size easily controlled by adjusting the thickness through nucleation and growth processes. It was observed that oxygen from the surrounding air permeated the Cu thin film through gaps between the Ag islands, leading to the oxidation of the Cu, particularly at the unstable GBs of uncoordinated Cu atoms. Consequently, smaller Cu grains with a higher GB density were prone to oxidation, which compromised the catalytic activity of the Cu–Ag thin-film catalyst. In contrast, a relatively thick Cu layer (≥80 nm) with a larger grain size effectively prevented oxidation, resulting in catalytic properties comparable to those of bulk Cu–Ag catalysts. Optimizing the Cu (100 nm) – Ag (3 nm) thin-film catalyst revealed a bifunctional characteristic. This catalyst could selectively produce both CO (FE_{CO} of 79.8%) and

CH₄ (FE_{CH_4} of 59.3%) at potentials of –1.0 and –1.4 V vs. RHE, respectively, as shown in Figure 9D,E. Furthermore, introducing a novel PEC architecture comprising the patterned Cu–Ag thin film, a SiO₂ passivation layer, and a p-Si photocathode, significantly improved the selectivity of CO and CH₄ under light illumination (100 mW cm⁻²). Cheng et al. explored the synthesis of CdS NPs featuring controllable S-vacancies encapsulated within a Zeolitic imidazolate framework-8 (ZIF-8) and utilized as a precursor for nitrogen-doped porous carbon (NCP) through a two-step process [111]. Initially, CdS NPs were stabilized with polyvinylpyrrolidone (PVP), followed by the deposition of a ZIF-8 shell onto their surface, resulting in a core-shell structure with the CdS NPs as the core and ZIF-8 as the shell. The subsequent control of S vacancies in the CdS and the pyridinic N content in the NCP was achieved through pyrolysis at various

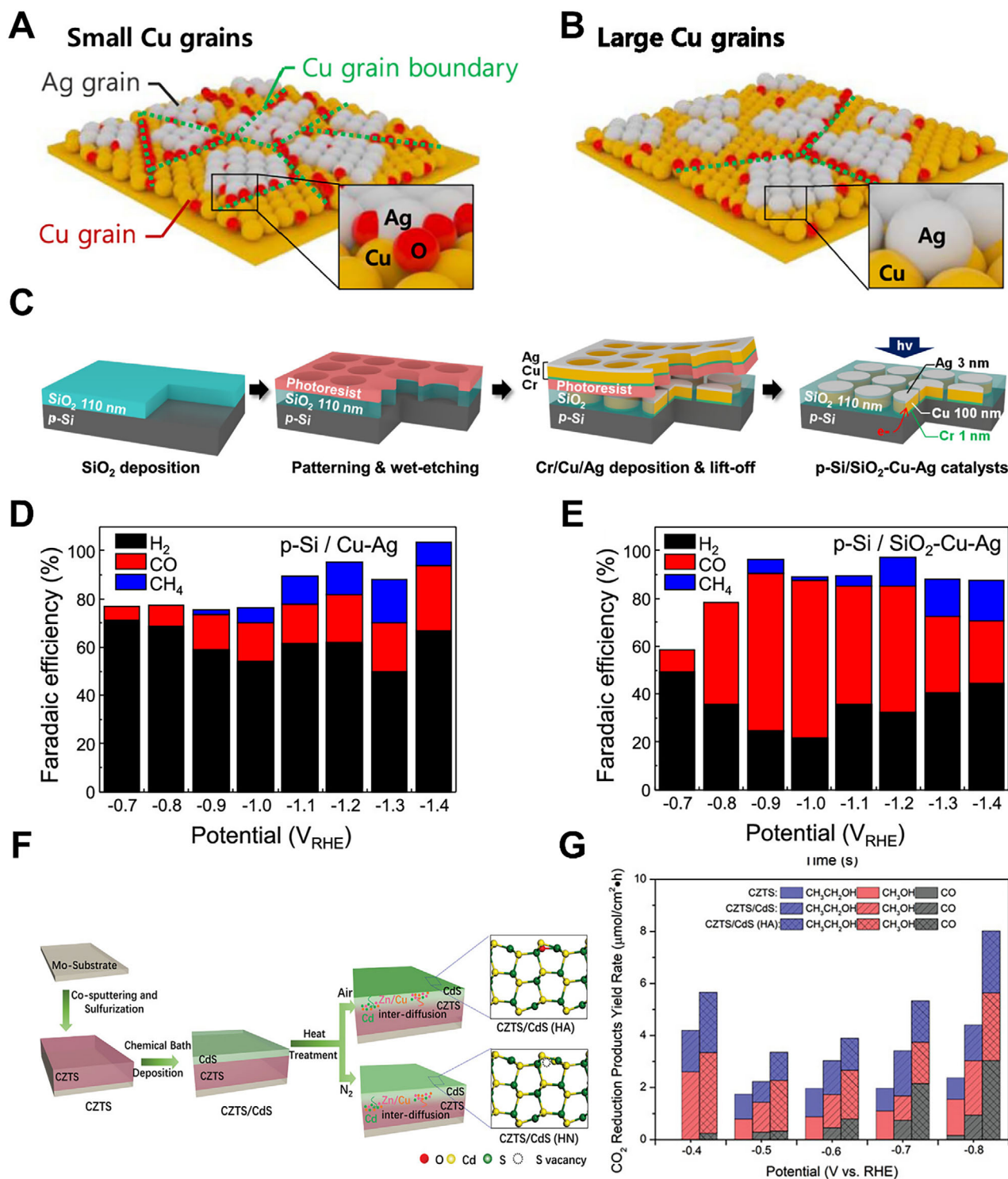


FIGURE 9 | Schematic illustrations of Cu-Ag thin-film cocatalyst with (A) small Cu grains and (B) large Cu grains. (C) Schematic depiction of fabrication procedures for the p-Si / SiO₂-Cu-Ag. FE_{total} from (D) p-Si/Cu-Ag and (E) p-Si / SiO₂-Cu-Ag. Reproduced with permission [110]. Copyright 2021, American Chemical Society. (F) Schematic fabrication processes of CZTS/CdS by different heat treatment conditions (Air or N₂ atmospheres). (G) CO₂RR products yield rate of CZTS, CZTS/CdS and CZTS/CdS (HA). Reproduced with permission [113]. Copyright 2021, John Wiley and Sons.

temperatures. The CdS/NCP catalysts, serving as cathodes with a TiO₂ nanotube array photoanode, enhanced the conductivity and stability of TMS-based catalysts and facilitated CO₂RR. Based on the pyrolysis temperature, the tunable S vacancies in the CdS/NCP samples led to enhanced selectivity towards CH₃OH,

which is attributed to the synergistic impact of S-vacancies in CdS and the pyridinic N content in nitrogen-doped porous carbon. The resulting CdS/NCP material, with its porous structure, abundant S-vacancies, high pyridinic N content, and enhanced conductivity, proved effective as a cathode catalyst for CO₂RR.

This synergistic effect was precisely controlled by adjusting the temperature (i.e., 300, 500, and 700°C) during the thermal treatment of the hybrid material. Notably, the sample treated at 500°C (CdS/NCP-500 catalyst) exhibited a high conversion rate (3052 nmol·h⁻¹·cm⁻²) with a selectivity of 77.3% towards CH₃OH.

Kan et al. ingeniously devised and crafted a p-Si/n-ZnO_v/p-Cu_xO heterostructure, incorporating a ZnO_v-derived Cu_xO defect level that exhibits a remarkable capability for selective PEC CO₂RR to C₂H₅OH at low biases [112]. The p-n-p band alignment was pivotal in confining and accumulating multiple electrons within the conduction band of n-type ZnO_v, facilitated by a built-in electric field. Simultaneously, the shallow ZnO_v defect level (vE_{ZnO_v}) allowed electrons to escape from the confined well and reach the Cu_xO (E_{Cu_xO}, 0.05 V vs. RHE). These tunneling defect energy levels on Cu_xO closely aligned with those required for the CO₂ to C₂H₅OH reduction, contributing to the heterostructure's exceptional selectivity for PEC CO₂RR towards C₂H₅OH at low biases, accompanied by an outstanding FE. In contrast, control samples, including p-Si/p-Cu_xO and p-Si/n-ZnO_v, necessitated higher overpotentials to overcome larger energy barriers, resulting in distinct CO₂RR selectivity towards CH₄ and HCOO⁻, respectively. The transfer of photoelectrons in the Si/ZnO_v/Cu_xO system was facilitated by a built-in electric field of approximately 0.6 V through a leaky tunnel formed in the defect levels of ZnO_v and Cu_xO, allowing for a close matching of energy levels and enabling the selective conversion of CO₂ into C₂H₅OH. The optimized potential and functional interface contributed to achieving an impressive FE exceeding 60% for PEC reduction of CO₂ to C₂H₅OH under 0 V vs. RHE. In addition to the prerequisites for efficient charge carrier transfer, studies have indicated that defect engineering plays a crucial role in regulating catalytic activity and CO₂RR selectivity based on the surface state of the photocatalyst. Nevertheless, the specific impact of sulfur vacancies on the transfer of photogenerated e⁻/h⁺ pairs and the reaction mechanism during CO₂RR remains unclear. Zhou et al. implemented a heat treatment strategy on Cu₂ZnSnS₄/CdS (CZTS/CdS) photocathodes, achieving simultaneous optimization of interface charge transfer and surface S vacancy engineering [113]. These advancements significantly contributed to the enhanced overall PEC CO₂RR performance and manageable selectivity. Heat treatment improved the CZTS/CdS heterojunction interface by promoting elemental inter-diffusion between Cd in CdS and Cu/Zn in CZTS, as shown in Figure 9F. This resulted in a more favorable p-n junction with an enlarged built-in potential, prolonged carrier lifetime, and suppressed charge recombination. Additionally, defects on the surface of CdS could be modulated through heat treatment in different atmospheres. Heat treatment in air replenished intrinsic S vacancies on the CZTS/CdS surface with oxygen, enhancing CO₂ and CO adsorption capability, as observed in Figure 9G, which leads to improved CO₂RR activity and higher selectivity toward CH₃OH/C₂H₅OH. Conversely, heat treatment in N₂ generated more S vacancies on the surface, facilitating surficial CO desorption and higher CO selectivity. By combining heterojunction design and modification of catalyst surface properties through a simple heat treatment strategy, this work established a new approach to designing photocathodes for high-performance PEC CO₂RR activity with controlled selectivity. Table 2 lists the performance of interface-engineered photocathodes for PEC CO₂RR.

4 | Conclusions and Perspectives

This review underscores the critical role of interface engineering in optimizing the efficiency of PEC photocathode, providing valuable insights into recent research trends, and contributing to the global pursuit of carbon neutrality. Interface engineering emerges as a pivotal strategy, optimizing cocatalysts, junction engineering, nanostructure engineering, and defect engineering to overcome existing limitations. Noble metal cocatalysts, such as Ag and Au, are seamlessly integrated with plasmonic materials to induce surface plasmon resonance, thereby enhancing light absorption and catalytic efficiency for PEC CO₂RR. This enhancement is evident in various studies utilizing diverse nanostructure and synthesis methods of plasmonic noble metal cocatalysts. Moreover, when semiconductor materials are integrated with various non-noble metal cocatalysts, they demonstrate promising advancements in enhancing electrocatalytic activity and selectivity for PEC CO₂RR. Semiconductor heterojunctions, encompassing type-I, type-II, and Schottky barrier junctions, play a pivotal role in enhancing PEC CO₂RR by facilitating the separation of photogenerated electrons and holes through distinct band structures. Nanostructure engineering further augments photocathode performance by manipulating materials on the nanometer scale, employing structures such as nanorods, nanowires, and core/shell configurations. Defect engineering, involving native point defects like vacancies and interstitials, influences catalytic, electrical, and optical properties. These defects, classified as 0D (point defects), 1D (line defects), 2D (interface defects), and 3D (bulk defects), enhance photoactivity in photocathode for PEC CO₂RR. Despite the numerous research outcomes, interface engineering still requires further studies. These studies should address the following issues:

- The PEC process based on interface engineering often involves complex procedures and expensive equipment, necessitating the development of more streamlined and cost-effective approaches.
- Extensive research is required to assess the long-term performance, stability, and durability of photocathode used in PEC CO₂RR experiments, particularly in challenging environmental conditions.
- Further research is required at the single photoelectrode level and beyond to achieve the ultimate goal of harnessing sunlight directly, without the need for additional external bias.
- Current investigations into PEC CO₂RR predominantly yield C₁ products; therefore, a critical need exists for comprehensive studies focusing on C₂₊ products, which offer higher value-added potential.

Researchers have made significant strides in addressing these challenges. Notably, the interface engineering of photocathode has demonstrated potential in improving PEC CO₂RR system performance by effectively capturing and segregating photogenerated charge carriers while minimizing recombination. Nevertheless, the implementation of interface engineering continues to present diverse challenges, including the complexity of the process, the necessity for stability, the requirement to advance to the device level, and the limited selectivity of the products. To achieve successful utilization of the PEC CO₂RR system, it is essential

TABLE 2 | Summary of the strategy for interface engineering of a photocathode for PEC CO₂RR.

Strategy	Photocathode materials	Electrolyte	Performance about activity and selectivity	Ref.
Plasmonic noble metal cocatalysts	CuBi ₂ O ₄ IOs-Ag	0.1 M KHCO ₃	FE _{CO} of 92%	[48]
	Au/TiO ₂ /n ⁺ p ⁻ Si	0.1 M KHCO ₃	<i>j</i> _{CO} of 5.52 mA cm ⁻² , FE _{CO} of 86%	[49]
	Ag-TiO ₂ /RGO	1.0 M KOH	<i>j</i> _{total} of 23.5 mA cm ⁻² , FE _{CH₃OH} of 60.5%	[50]
	Au/α-Fe ₂ O ₃ /RGO	0.1 M KOH	<i>j</i> _{total} of -31.5 mA cm ⁻² , FE _{CH₃OH} of 21.5%	[51]
	Ag/Cu-TS-1	0.1 M KHCO ₃	C ₂ H ₅ OH yield rate of 2.62 μmol cm ⁻² h ⁻¹	[52]
	Cu ₂ O/Ag	0.1 M KHCO ₃	Yield rate of 212.7 μmol cm ⁻² h ⁻¹ , FE _{CH₃COOH} of 47.7%	[53]
Non-noble metal cocatalysts	STA-GO/CoPc	0.1 M KHCO ₃	<i>j</i> _{total} of 0.7 mA cm ⁻² , FE _{CO} of 86%, FE _{CH₃OH} of 8%	[62]
	Si mesoTiO ₂ CoPcP	0.5 M KHCO ₃	TONco of 939 ± 132, FE _{CO} of 66%	[63]
	Si TiO ₂ CNT Co ^{II} (BrqPy)	0.1 M KHCO ₃	<i>j</i> _{total} of -1.4 mA cm ⁻² , FE _{CO} of 97%	[64]
	Si mesoTiO ₂ CotpyP	MeCN with 0.1 M TBABF ₄	TON of 381	[65]
	CuS/GaN/Si	0.1 M KHCO ₃	<i>j</i> _{HCOOH} of 7.07 mA cm ⁻² , FE _{HCOOH} of 70.2%	[66]
	Bi/GaN/Si	0.1 M KHCO ₃	<i>j</i> _{HCOOH} of 10.3 mA cm ⁻² , FE _{HCOOH} of 98%	[67]
	Sn NP/GaN NW/Si	0.1 M KHCO ₃	<i>j</i> _{total} of 17.5 mA cm ⁻² , FE _{HCOOH} of 76.9%	[68]
	Cu ₃ (BTC) ₂ /Cu ₂ O	MeCN with 0.1 M TBAPF ₆	FE _{CO} of about 95%	[69]
	CuN _x /CuO	0.1 M KHCO ₃	<i>j</i> _{total} of -1.0 mA cm ⁻² , FE _{C₂} of 15.2%	[70]
	Cu NPs/Si NWs	0.1 M KHCO ₃	<i>j</i> _{C₂H₄} exceeding 2.5 mA cm ⁻² , FE _{C₂H₄} of about 25%	[71]
	Cu/TiO ₂ /p-Si	0.1 M CsHCO ₃	<i>j</i> _{C₂H₄} of -2.3 mA cm ⁻²	[72]
	Bi@ZFO NTs	0.1 M KHCO ₃	FE _{HCOOH} of 61.2%	[74]
Junction engineering	CuO/g-C ₃ N ₄ /carbon paper	0.1 M NaHCO ₃	FE _{CH₃OH} of 75%	[75]
	CeO ₂ NPs/CuO NPs/Cu	0.1 M KHCO ₃	CH ₃ OH yield rate of 3.44 μmol cm ⁻² h ⁻¹ , FE _{CH₃OH} of 60%	[76]
	ZnPc/carbon nitride	0.1 M KHCO ₃	CH ₃ OH yield of 13 μmol L ⁻¹	[77]
	CdS-CuFe ₂ O ₄	0.1 M NaHCO ₃	CH ₃ OH yield of 23.8 μmol L ⁻¹ cm ⁻² , FE _{CH₃OH} of 72%	[78]
	Pd@TiO ₂ /Ti ₃ CN	0.1 M KHCO ₃	yield rate of 45.6 μM cm ⁻² h ⁻¹	[79]
	CuFeO ₂ /CuO nanowire	Triethanolamine	FE _{C₂H₅OH} of 66.73%	[80]
	CuFeO ₂ /TNNTs	0.1 M NaHCO ₃	<i>j</i> _{total} of 80 μA cm ⁻² , C ₂ H ₅ OH yield rate of 3.3 μmol/5h·cm ⁻²	[81]
	BCW-6	0.1 M KHCO ₃	C ₂ H ₅ OH yield rate of 600 μmol h ⁻¹ g ⁻¹ , FE _{C₂H₅OH} of 80%	[82]
	g-C ₃ N ₄ /ZnTe	0.1 M KHCO ₃	C ₂ H ₅ OH yield rate of 17.1 μmol cm ⁻² h ⁻¹	[83]
	Zn _x :Co _y @Cu	0.1 M KHCO ₃	paraffin yield rate of 325 μg h ⁻¹	[84]
	Au-TiO ₂ /InP	0.1 M KHCO ₃	FE _{CO} of 84.2%	[94]
	b-Au ₁ /Si	0.1 M KHCO ₃	<i>j</i> _{total} of -13.1 mA cm ⁻² , FE _{CO} of 82.2%	[95]
Nanosturcture engineering	TO600	1 M KOH	HCOOH yield rate of 165 μmol cm ⁻² h ⁻¹ , FE _{HCOOH} of 64%	[96]
	Ag/WO ₃ -NR	0.1 M KHCO ₃	<i>j</i> _{HCOO⁻} of 0.4 mA cm ⁻² , HCOO ⁻ yield rate of 31.7 mmol h ⁻¹	[97]

(Continues)

TABLE 2 | (Continued)

Strategy	Photocathode materials	Electrolyte	Performance about activity and selectivity	Ref.
	Ag-supported dendritic Cu	0.1 M CsHCO ₃	FE _{C₂₊} of 60%	[98]
	n ⁺ p ⁻ Si μW/Cu	0.1 M KHCO ₃	j_{CH_4} of $2.9 \pm 0.7 \text{ mA cm}^{-2}$, $j_{\text{C}_2\text{H}_4}$ of $2.1 \pm 0.2 \text{ mA cm}^{-2}$	[99]
Defect engineering	Cu–Ag thin film	0.1 M KHCO ₃	FE _{CO} of 79.8%, FE _{CH₄} of 59.3%	[110]
	CdS/NCP	0.5 M KHCO ₃	FE _{CH₃OH} of 77.3%	[111]
	p-Si/n-ZnO _v /p-Cu _x O	0.1 M KHCO ₃	FE _{C₂H₅OH} of exceeding 60%	[112]
	CZTS/CdS	0.1 M KHCO ₃	CO yield rate of $2.31 \mu\text{mol cm}^{-2} \text{ h}^{-1}$	[113]

to develop a more sophisticated and facile interface engineering technique that can effectively address the aforementioned challenges. The incorporation of suitable interlayers, transport layers, and electron-blocking layers is essential for enhancing stability of photocathode. The design of efficient configurations with multijunction photocathodes represents an effective means of enhancing photocathode utilization and overall efficiency. The cocatalysts play an electrochemically pivotal role in promoting desired PEC CO₂RR, with Cu cocatalysts being particularly effective in producing C₂₊ products. The integration of these cocatalysts into composite materials and the modification of their structure can facilitate the production of various C₂₊ products.

In conclusion, this review paper examines the current trends of research on photocathode for PEC CO₂RR from the perspective of interface engineering. By identifying these trends, the paper aims to make a significant contribution to the broader field of CO₂RR research.

Acknowledgments

This research was supported by the National Research Foundation of Korea (NRF), funded by the Korean government (2022M3H4A1A01012712, 2022M3H4A1A04096380).

Conflicts of Interest Statement

The authors declare no conflicts of interest.

References

1. T. R. Anderson, E. Hawkins, and P. D. Jones, "CO₂, the Greenhouse Effect and Global Warming: From the Pioneering Work of Arrhenius and Callendar to Today's Earth System Models," *Endeavour* 40 (2016): 178.
2. Y. Xie, T. T. Wang, X. H. Liu, K. Zou, and W. Q. Deng, "Capture and Conversion of CO₂ at Ambient Conditions by a Conjugated Microporous Polymer," *Nature Communications* 4 (2013): 1960.
3. S. Xiang, Y. He, Z. Zhang, et al., "Microporous Metal-organic Framework With Potential for Carbon Dioxide Capture at Ambient Conditions," *Nature Communications* 3 (2012): 954.
4. Z. Liu, Z. Deng, B. Zhu, et al., "Global Patterns of Daily CO₂ Emissions Reductions in the First Year of COVID-19," *Nature Geoscience* 15 (2022): 615.
5. V. Masson-Delmotte, P. Zhai, A. Pirani, et al., *IPCC, 2021: Climate Change 2021: The Physical Science Basis. Contribution of Working Group*

I to the Sixth Assessment Report of the Intergovernmental Panel on Climate Change (Cambridge University Press, 2021), 2391.

6. Z. Liu, Z. Deng, S. Davis, and P. Ciaia, "Monitoring Global Carbon Emissions in 2022," *Nature Reviews Earth & Environment* 4 (2023): 205.
7. Y. R. Wang, Q. Huang, C. T. He, et al., "Oriented Electron Transmission in Polyoxometalate-Metalloporphyrin Organic Framework for Highly Selective Electroreduction of CO₂," *Nature Communications* 9 (2018): 4466.
8. N. T. Nesbitt, M. Ma, B. J. Trzeźniewski, et al., "Au Dendrite Electrocatalysts for CO₂ Electrolysis," *Journal of Physical Chemistry C* 122 (2018): 10006.
9. Y. T. Guntern, J. R. Pankhurst, J. Vavra, et al., "Nanocrystal/Metal–Organic Framework Hybrids as Electrocatalytic Platforms for CO₂ Conversion," *Angewandte Chemie* 131 (2019): 12762.
10. L. K. Putri, W. J. Ong, W. S. Chang, and S. P. Chai, "Enhancement in the Photocatalytic Activity of Carbon Nitride Through Hybridization With Light-Sensitive AgCl for Carbon Dioxide Reduction to Methane," *Catalysis Science & Technology* 6 (2016): 744.
11. X. Y. Kong, T. Tong, B. J. Ng, et al., "Topotactic Transformation of Bismuth Oxybromide Into Bismuth Tungstate: Bandgap Modulation of Single-Crystalline {001}-Faceted Nanosheets for Enhanced Photocatalytic CO₂ Reduction," *ACS Appl Mater Interfaces* 12 (2020): 26991.
12. X. Y. Kong, Y. Y. Choo, S. P. Chai, A. K. Soh, and A. R. Mohamed, "Oxygen Vacancy Induced Bi₂WO₆ for the Realization of Photocatalytic CO₂ Reduction Over the Full Solar Spectrum: From the UV to the NIR Region," *Chemical Communications* 52 (2016): 14242.
13. X. Y. Kong, W. L. Tan, B. J. Ng, S. P. Chai, and A. R. Mohamed, "Harnessing Vis–NIR Broad Spectrum for Photocatalytic CO₂ Reduction Over Carbon Quantum Dots-decorated Ultrathin Bi₂WO₆ Nanosheets," *Nano Research* 10 (2017): 1720.
14. Z. Yang, Y. Qi, F. Wang, et al., "State-of-the-art Advancements in Photo-assisted CO₂ Hydrogenation: Recent Progress in Catalyst Development and Reaction Mechanisms," *Journal of Materials Chemistry A* 8 (2020): 24868.
15. T. Kulandaivalu, A. R. Mohamed, K. A. Ali, and M. Mohammadi, "Photocatalytic Carbon Dioxide Reforming of Methane as an Alternative Approach for Solar Fuel Production—a Review," *Renewable & Sustainable Energy Reviews* 134 (2020): 110363.
16. T. Amrillah, A. R. Supandi, V. Puspasari, A. Hermawan, and Z. W. Seh, "MXene-Based Photocatalysts and Electrocatalysts for CO₂ Conversion to Chemicals," *Transactions of Tianjin University* 28 (2022): 307.
17. J. H. Cho, J. Ma, and S. Y. Kim, "Toward High-Efficiency Photovoltaics-Assisted Electrochemical and Photoelectrochemical CO₂ Reduction: Strategy and Challenge," *Exploration* 3 (2023): 20230001.
18. D. Yang, H. Yu, T. He, et al., "Visible-light-switched Electron Transfer Over Single Porphyrin-metal Atom Center for Highly Selective

- Electroreduction of Carbon Dioxide," *Nature Communications* 10 (2019): 3844.
19. G. H. Han, J. Bang, G. Park, et al., "Recent Advances in Electrochemical, Photochemical, and Photoelectrochemical Reduction of CO₂ to C₂+ Products," *Small* 19 (2023): 2205765.
 20. R. Kortlever, J. Shen, K. J. P. Schouten, F. Calle-Vallejo, and M. T. Koper, "Catalysts and Reaction Pathways for the Electrochemical Reduction of Carbon Dioxide," *Journal of Physical Chemistry Letters* 6 (2015): 4073.
 21. J. T. Feaster, C. Shi, E. R. Cave, et al., "Understanding Selectivity for the Electrochemical Reduction of Carbon Dioxide to Formic Acid and Carbon Monoxide on Metal Electrodes," *ACS Catalysis* 7 (2017): 4822.
 22. A. Bagger, W. Ju, A. S. Varela, P. Strasser, and J. Rossmeisl, "Electrochemical CO₂ Reduction: A Classification Problem," *Chemphyschem* 18 (2017): 3266.
 23. J. Santatiwongchai, K. Faungnawakij, and P. Hirunsit, "Comprehensive Mechanism of CO₂ Electroreduction Toward Ethylene and Ethanol: The Solvent Effect From Explicit Water-Cu(100) Interface Models," *ACS Catalysis* 11 (2021): 9688.
 24. M. Halmann, "Photoelectrochemical Reduction of Aqueous Carbon Dioxide on p-Type Gallium Phosphide in Liquid Junction Solar Cells," *Nature* 275 (1978): 115.
 25. V. H. Nguyen, B. S. Nguyen, Z. Jin, et al., "Towards Artificial Photosynthesis: Sustainable Hydrogen Utilization for Photocatalytic Reduction of CO₂ to High-Value Renewable Fuels," *Journal of Chemical Engineering* 402 (2020): 126184.
 26. T. P. Nguyen, D. L. T. Nguyen, V. H. Nguyen, et al., "Recent Advances in TiO₂-Based Photocatalysts for Reduction of CO₂ to Fuels," *Nanomaterials* 10 (2020): 337.
 27. H. H. Do, D. L. T. Nguyen, X. C. Nguyen, et al., "Recent Progress in TiO₂-based Photocatalysts for Hydrogen Evolution Reaction: A Review," *Arabian Journal of Chemistry* 13 (2020): 3653.
 28. S. Thiele, J. Bachmann, and S. Cherevko, "Dissolution of WO₃ Modified With IrOx Overlayers During Photoelectrochemical Water Splitting," *SusMat* 3 (2023): 128.
 29. P. Ding, T. Jiang, N. Han, and Y. Li, "Photocathode Engineering for Efficient Photoelectrochemical CO₂ Reduction," *Materials Today Nano* 10 (2020): 100077.
 30. W. Zhang, Z. Jin, and Z. Chen, "Rational-Designed Principles for Electrochemical and Photoelectrochemical Upgrading of CO₂ to Value-Added Chemicals," *Advancement of Science* 9 (2022): 2105204.
 31. A. U. Pawar, C. W. Kim, M.-T. Nguyen-Le, and Y. S. Kang, "General Review on the Components and Parameters of Photoelectrochemical System for CO₂ Reduction With In Situ Analysis," *ACS Sustainable Chemistry & Engineering* 7 (2019): 7431.
 32. Y. Deng and B. S. Yeo, "Characterization of Electrocatalytic Water Splitting and CO₂ Reduction Reactions Using In Situ/Operando Raman Spectroscopy," *ACS Catalysis* 7 (2017): 7873.
 33. M. J. Kang, C. W. Kim, A. U. Pawar, et al., "Selective Alcohol on Dark Cathodes by Photoelectrochemical CO₂ Valorization and Their In Situ Characterization," *ACS Energy Letters* 4 (2019): 1549.
 34. H. Gong, Z. Wei, Z. Gong, et al., "Low-Coordinated Co-N-C on Oxygenated Graphene for Efficient Electrocatalytic H₂O₂ Production," *Advanced Functional Materials* 32 (2022): 2106886.
 35. J. Ma, J. H. Cho, C. Lee, et al., "Unraveling the Harmonious Coexistence of Ruthenium States on a Self-Standing Electrode for Enhanced Hydrogen Evolution Reaction," *Energy & Environmental Materials* 7 (2024): e12766.
 36. Y. Sun, S. Ding, B. Xia, J. Duan, M. Antonietti, and S. Chen, "Biomimetic FeMo(Se, Te) as Joint Electron Pool Promoting Nitrogen Electrofixation," *Angewandte Chemie* 134 (2022): e202115198.
 37. A. Molinari, L. Samiolo, and R. Amadelli, "EPR Spin Trapping Evidence of Radical Intermediates in the Photo-reduction of Bicarbonate/CO₂ in TiO₂ Aqueous Suspensions," *Photochemical & Photobiological Sciences* 14 (2015): 1039.
 38. J. Ma, S. H. Ahn, and S. Y. Kim, "Integration of Earth-abundant Cocatalysts for High-performance Photoelectrochemical Energy Conversion," *Journal of Energy Chemistry* 88 (2024): 336.
 39. J. Liu, C. Xia, S. Zaman, Y. Su, L. Tan, and S. Chen, "Surface Plasmon Assisted Photoelectrochemical Carbon Dioxide Reduction: Progress and Perspectives," *Journal of Materials Chemistry A* 11 (2023): 16918.
 40. K. Watanabe, D. Menzel, N. Nilius, and H. J. Freund, "Photochemistry on Metal Nanoparticles," *Chemical Reviews* 106 (2006): 4301.
 41. S. Linic, P. Christopher, and D. B. Ingram, "Plasmonic-metal Nanostructures for Efficient Conversion of Solar to Chemical Energy," *Nature Materials* 10 (2011): 911.
 42. G. Baffou and R. Quidant, "Nanoplasmonics for Chemistry," *Chemical Society Reviews* 43 (2014): 3898.
 43. U. Aslam, V. G. Rao, S. Chavez, and S. Linic, "Catalytic Conversion of Solar to Chemical Energy on Plasmonic Metal Nanostructures," *Nature Catalysis* 1 (2018): 656.
 44. S. Chen, W. H. Li, W. Jiang, et al., "MOF Encapsulating N-Heterocyclic Carbene-Ligated Copper Single-Atom Site Catalyst towards Efficient Methane Electrosynthesis," *Angewandte Chemie International Edition* 134 (2022): e202114450.
 45. V. H. Nguyen, B. S. Nguyen, and C. C. Hu, "Novel Architecture Titanium Carbide (Ti₃C₂T_x) MXene Cocatalysts Toward Photocatalytic Hydrogen Production: A Mini-Review," *Nanomaterials* 10 (2020): 602.
 46. S. Bae, S. Lee, H. Ryu, and W. J. Lee, "Improvement of Photoelectrochemical Properties of CuO Photoelectrode by Li Doping," *Korean Journal of Metals and Materials* 60 (2022): 577.
 47. V. Kumar, R. K. Mishra, L. G. Trung, et al., "Copper, Palladium, and Reduced Graphene Oxide co-doped Layered WS₂/WO₃ Nanostructures for Electrocatalytic Hydrogen Generation," *Electronic Materials Letters* 20 (2024): 414.
 48. G. Liu, R. Cai, Z. Lv, et al., "Ameliorating the Carrier Dynamics Behavior via Plasmonic Ag-modified CuBi₂O₄ Inverse Opal for the Efficient Photoelectrocatalytic Reduction of CO₂ to CO," *Journal of Catalysis* 424 (2023): 130.
 49. K. Wang, N. Fan, B. Xu, et al., "Steering the Pathway of Plasmon-Enhanced Photoelectrochemical CO₂ Reduction by Bridging Si and Au Nanoparticles Through a TiO₂ Interlayer," *Small* 18 (2022): 2201882.
 50. G. Bharath, J. Prakash, K. Rambabu, et al., "Synthesis of TiO₂/RGO With Plasmonic Ag Nanoparticles for Highly Efficient Photoelectrocatalytic Reduction of CO₂ to Methanol Toward the Removal of an Organic Pollutant From the Atmosphere," *Environmental Pollution* 281 (2021): 116990.
 51. G. Bharath, K. Rambabu, A. Hai, et al., "Dual-functional Paired Photoelectrocatalytic System for the Photocathodic Reduction of CO₂ to Fuels and the Anodic Oxidation of Furfural to Value-Added Chemicals," *Applied Catalysis B* 298 (2021): 120520.
 52. G. Li, M. Wang, H. Shao, et al., "Light-Driven Carbon Dioxide Reduction Over the Ag-Decorated Modified TS-1 Zeolite," *Catalysis Science & Technology* 12 (2022): 2490.
 53. Y. Zhang, Q. Wang, K. Wang, et al., "Plasmonic Ag-decorated Cu₂O Nanowires for Boosting Photoelectrochemical CO₂ Reduction to Multi-Carbon Products," *Chemical Communications* 58 (2022): 9421.
 54. L. K. Putri, B. J. Ng, W. J. Ong, S. P. Chai, and A. R. Mohamed, "Toward Excellence in Photocathode Engineering for Photoelectrochemical CO₂ Reduction: Design Rationales and Current Progress," *Advanced Energy Materials* 12 (2022): 2201093.
 55. J. C. Matsubu, E. T. Lin, K. L. Gunther, K. N. Bozhilov, Y. Jiang, and P. Christopher, "Critical Role of Interfacial Effects on the Reactivity of

- Semiconductor-cocatalyst Junctions for Photocatalytic Oxygen Evolution From Water," *Catalysis Science & Technology* 6 (2016): 6836.
56. C. Shi, H. A. Hansen, A. C. Lausche, and J. K. Nørskov, "Trends in Electrochemical CO₂ Reduction Activity for Open and Close-packed Metal Surfaces," *Physical Chemistry Chemical Physics* 16 (2014): 4720.
57. Y. Sun, X. Liu, M. Zhu, et al., "Non-Noble Metal Single Atom-Based Catalysts for Electrochemical Reduction of CO₂: Synthesis Approaches and Performance Evaluation," *DeCarbon* 2 (2023): 100018.
58. P. Rao, Y. Yu, S. Wang, et al., "Understanding the Improvement Mechanism of Plasma Etching Treatment on Oxygen Reduction Reaction Catalysts," *Exploration* 4 (2024): 20230034.
59. S. K. Choi, U. Kang, S. Lee, D. J. Ham, S. M. Ji, and H. Park, "Sn-Coupled p-Si Nanowire Arrays for Solar Formate Production From CO₂," *Advanced Energy Materials* 4 (2014): 1301614.
60. Q. Shen, Z. Chen, X. Huang, M. Liu, and G. Zhao, "High-Yield and Selective Photoelectrocatalytic Reduction of CO₂ to Formate by Metallic Copper Decorated Co₃O₄ Nanotube Arrays," *Environmental Science & Technology* 49 (2015): 5828.
61. K. Alenezi, S. K. Ibrahim, P. Li, and C. J. Pickett, "Solar Fuels: Photoelectrosynthesis of CO From CO₂ at p-Type Si Using Fe Porphyrin Electrocatalysts," *Chemistry – A European Journal* 19 (2013): 13522.
62. B. Shang, C. L. Rooney, D. J. Gallagher, et al., "Aqueous Photoelectrochemical CO₂ Reduction to CO and Methanol Over a Silicon Photocathode Functionalized With a Cobalt Phthalocyanine Molecular Catalyst," *Angewandte Chemie* 135 (2023): e202215213.
63. S. Roy, M. Miller, J. Warnan, J. J. Leung, C. D. Sahm, and E. Reisner, "Electrocatalytic and Solar-Driven Reduction of Aqueous CO₂ With Molecular Cobalt Phthalocyanine–Metal Oxide Hybrid Materials," *ACS Catalysis* 11 (2021): 1868.
64. Z. Wen, S. Xu, Y. Zhu, et al., "Aqueous CO₂ Reduction on Si Photocathodes Functionalized by Cobalt Molecular Catalysts/Carbon Nanotubes," *Angewandte Chemie* 134 (2022): e202201086.
65. J. J. Leung, J. Warnan, K. H. Ly, et al., "Solar-Driven Reduction of Aqueous CO₂ With a Cobalt Bis(Terpyridine)-Based Photocathode," *Nat Catalysis* 2 (2019): 354.
66. W. J. Dong, I. A. Navid, Y. Xiao, J. W. Lim, J. L. Lee, and Z. Mi, "CuS-Decorated GaN Nanowires on Silicon Photocathodes for Converting CO₂ Mixture Gas to HCOOH," *Journal of the American Chemical Society* 143 (2021): 10099.
67. W. J. Dong, I. A. Navid, Y. Xiao, et al., "Bi Catalysts Supported on GaN Nanowires Toward Efficient Photoelectrochemical CO₂ Reduction," *Journal of Materials Chemistry A* 10 (2022): 7869.
68. B. Zhou, X. Kong, S. Vanka, et al., "A GaN:Sn Nanoarchitecture Integrated on a Silicon Platform for Converting CO₂ to HCOOH by Photoelectrocatalysis," *Energy & Environmental Science* 12 (2019): 2842.
69. X. Deng, R. Li, S. Wu, et al., "Metal–Organic Framework Coating Enhances the Performance of Cu₂O in Photoelectrochemical CO₂ Reduction," *Journal of the American Chemical Society* 141 (2019): 10924.
70. K. Wang, Y. Liu, Q. Wang, et al., "Asymmetric Cu–N Sites on Copper Oxide Photocathode for Photoelectrochemical CO₂ Reduction towards C₂ Products," *Applied Catalysis B* 316 (2022): 121616.
71. I. Roh, S. Yu, C. K. Lin, S. Louisia, S. Cestellos-Blanco, and P. Yang, "Photoelectrochemical CO₂ Reduction Toward Multicarbon Products With Silicon Nanowire Photocathodes Interfaced With Copper Nanoparticles," *Journal of the American Chemical Society* 144 (2022): 8002.
72. C. Kim, A. J. King, S. Aloni, F. M. Toma, A. Z. Weber, and A. T. Bell, "Codesign of an Integrated Metal–Insulator–Semiconductor Photocathode for Photoelectrochemical Reduction of CO₂ to Ethylene," *Energy & Environmental Science* 16 (2023): 2968.
73. L. Liu, Y. Zhang, and H. Huang, "Junction Engineering for Photocatalytic and Photoelectrocatalytic CO₂ Reduction," *Solar RRL* 5 (2021): 2000430.
74. T. Ouyang, Y. Q. Ye, C. Tan, et al., "1D α -Fe₂O₃ /ZnO Junction Arrays Modified by Bi as Photocathode: High Efficiency in Photoelectrochemical Reduction of CO₂ to HCOOH," *Journal of Physical Chemistry Letters* 13 (2022): 6867.
75. X. X. Jiang, X. De Hu, M. Tarek, et al., "Tailoring the Properties of G-C₃N₄ With CuO for Enhanced Photoelectrocatalytic CO₂ Reduction to Methanol," *Journal of CO₂ Utilization* 40 (2020): 101222.
76. Z. Pan, E. Han, J. Zheng, et al., "Highly Efficient Photoelectrocatalytic Reduction of CO₂ to Methanol by a p–n Heterojunction CeO₂/CuO/Cu Catalyst," *Nano-Micro Letters* 12 (2020): 18.
77. J. Zheng, X. Li, Y. Qin, et al., "Zn Phthalocyanine/Carbon Nitride Heterojunction for Visible Light Photoelectrocatalytic Conversion of CO₂ to Methanol," *Journal of Catalysis* 371 (2019): 214.
78. M. Tarek, K. M. R. Karim, S. M. Sarkar, et al., "Hetero-structure CdS–CuFe₂O₄ as an Efficient Visible Light Active Photocatalyst for Photoelectrochemical Reduction of CO₂ to Methanol," *International Journal of Hydrogen Energy* 44 (2019): 26271.
79. Y. Xu, F. Wang, S. Lei, et al., "In Situ Grown Two-dimensional TiO₂/Ti₃CN MXene Heterojunction Rich in Ti³⁺ Species for Highly Efficient Photoelectrocatalytic CO₂ Reduction," *Journal of Chemical Engineering* 452 (2023): 139392.
80. M. Lu, D. Jia, H. Xue, J. Tian, and T. Jiang, "0D/1D CuFeO₂/CuO Nanowire Heterojunction Arrays for Improved Photoelectrocatalytic Reduction of CO₂ to Ethanol," *Journal of Alloys and Compounds* 960 (2023): 170626.
81. L. Zhang, H. Cao, Y. Lu, et al., "Effective Combination of CuFeO₂ With High Temperature Resistant Nb-doped TiO₂ Nanotube Arrays for CO₂ Photoelectric Reduction," *Journal of Colloid & Interface Science* 568 (2020): 198.
82. J. Wang, Y. Wei, B. Yang, B. Wang, J. Chen, and H. Jing, "In Situ Grown Heterojunction of Bi₂WO₆/BiOCl for Efficient Photoelectrocatalytic CO₂ Reduction," *Journal of Catalysis* 377 (2019): 209.
83. Q. Wang, X. Wang, Z. Yu, et al., "Artificial Photosynthesis of Ethanol Using Type-II G-C₃N₄/ZnTe Heterojunction in Photoelectrochemical CO₂ Reduction System," *Nano Energy* 60 (2019): 827.
84. J. Wang, Y. Guan, X. Yu, et al., "Photoelectrocatalytic Reduction of CO₂ to Paraffin Using Pn Heterojunctions," *iScience* 23 (2020): 100768.
85. J. Luo, L. Steier, M. K. Son, M. Schreier, M. T. Mayer, and M. Grätzel, "Cu₂O Nanowire Photocathodes for Efficient and Durable Solar Water Splitting," *Nano Letters* 16 (2016): 1848.
86. M. A. Rahman, J. P. Thomas, and K. T. Leung, "A Delaminated Defect-Rich ZrO₂ Hierarchical Nanowire Photocathode for Efficient Photoelectrochemical Hydrogen Evolution," *Advanced Energy Materials* 8 (2018): 1701234.
87. C. A. Bignozzi, S. Caramori, V. Cristino, R. Argazzi, L. Meda, and A. Tacca, "Nanostructured Photoelectrodes Based on WO₃: Applications to Photooxidation of Aqueous Electrolytes," *Chemical Society Reviews* 42 (2013): 2228.
88. J. Pan, G. Liu, G. Q. Lu, and H. M. Cheng, "On the True Photoreactivity Order of {001}, {010}, and {101} Facets of Anatase TiO₂ Crystals," *Angewandte Chemie International Edition* 50 (2011): 2133.
89. G. Liu, L. C. Yin, J. Pan, et al., "Greatly Enhanced Electronic Conduction and Lithium Storage of Faceted TiO₂ Crystals Supported on Metallic Substrates by Tuning Crystallographic Orientation of TiO₂," *Advanced Materials* 27 (2015): 3507.
90. S. Selcuk and A. Selloni, "Facet-dependent Trapping and Dynamics of Excess Electrons at Anatase TiO₂ Surfaces and Aqueous Interfaces," *Nature Materials* 15 (2016): 1107.
91. M. Zhao, H. Xu, H. Chen, et al., "Photocatalytic Reactivity of {121} and {211} Facets of Brookite TiO₂ Crystals," *Journal of Materials Chemistry A* 3 (2015): 2331.

92. Y. Li, X. Yun, H. Chen, W. Zhang, and Y. Li, "Facet-Selective Charge Carrier Transport, Deactivation Mechanism and Stabilization of a Cu₂O Photo-Electro-Catalyst," *Physical Chemistry Chemical Physics* 18 (2016): 7023.
93. N. Li, M. Liu, Z. Zhou, J. Zhou, Y. Sun, and L. Guo, "Charge Separation in Facet-engineered Chalcogenide Photocatalyst: A Selective Photocorrosion Approach," *Nanoscale* 6 (2014): 9695.
94. G. Liu, P. R. Narangari, Q. T. Trinh, et al., "Manipulating Intermediates at the Au-TiO₂ Interface Over InP Nanopillar Array for Photoelectrochemical CO₂ Reduction," *ACS Catalysis* 11 (2021): 11416.
95. J. Hu, N. Fan, C. Chen, et al., "Facet Engineering in Au Nanoparticles Buried in p-Si Photocathodes for Enhanced Photoelectrochemical CO₂ Reduction," *Applied Catalysis B* 327 (2023): 122438.
96. S. Mubarak, D. Dhamodharan, H. S. Byun, S. B. Arya, and D. K. Pattanayak, "Effective Photoelectrocatalytic Reduction of CO₂ to Formic Acid Using Controllably Annealed TiO₂ Nanoparticles Derived From Porous Structured Ti Foil," *Journal of CO₂ Utilization* 63 (2022): 102152.
97. B. Paul, N. Manwar, P. Bhanja, et al., "Morphology Controlled Synthesis of 2D Heterostructure Ag/WO₃ Nanocomposites for Enhanced Photoelectrochemical CO₂ Reduction Performance," *Journal of CO₂ Utilization* 41 (2020): 101284.
98. J. W. Beeman, J. Bullock, H. Wang, et al., "Si Photocathode With Ag-Supported Dendritic Cu Catalyst for CO₂ Reduction," *Energy & Environmental Science* 12 (2019): 1068.
99. P. A. Kempler, M. H. Richter, W. H. Cheng, B. S. Brunshwig, and N. S. Lewis, "Si Microwire-Array Photocathodes Decorated With Cu Allow CO₂ Reduction With Minimal Parasitic Absorption of Sunlight," *ACS Energy Letters* 5 (2020): 2528.
100. J. C. Wu, J. Zheng, P. Wu, and R. Xu, "Study of Native Defects and Transition-Metal (Mn, Fe, Co, and Ni) Doping in a Zinc-Blende CdS Photocatalyst by DFT and Hybrid DFT Calculations," *Journal of Physical Chemistry C* 115 (2011): 5675.
101. B. Zhang, L. Wang, Y. Zhang, Y. Ding, and Y. Bi, "Ultrathin FeOOH Nanolayers With Abundant Oxygen Vacancies on BiVO₄ Photoanodes for Efficient Water Oxidation," *Angewandte Chemie International Edition* 57 (2018): 2248.
102. D. Liu, Y. Lv, M. Zhang, et al., "Defect-related Photoluminescence and Photocatalytic Properties of Porous ZnO Nanosheets," *Journal of Materials Chemistry A* 2 (2014): 15377.
103. H. Wu, F. Meng, L. Li, S. Jin, and G. Zheng, "Dislocation-Driven CdS and CdSe Nanowire Growth," *ACS Nano* 6 (2012): 4461.
104. S. W. Lee, S. Chen, W. Sheng, et al., "Roles of Surface Steps on Pt Nanoparticles in Electro-oxidation of Carbon Monoxide and Methanol," *Journal of the American Chemical Society* 131 (2009): 15669.
105. J. Yan, G. Wu, N. Guan, L. Li, Z. Li, and X. Cao, "Understanding the Effect of Surface/Bulk Defects on the Photocatalytic Activity of TiO₂: Anatase versus Rutile," *Physical Chemistry Chemical Physics* 15 (2013): 10978.
106. M. Kong, Y. Li, X. Chen, et al., "Tuning the Relative Concentration Ratio of Bulk Defects to Surface Defects in TiO₂ Nanocrystals Leads to High Photocatalytic Efficiency," *Journal of the American Chemical Society* 133 (2011): 16414.
107. R. Qu, W. Zhang, N. Liu, et al., "Antioil Ag₃PO₄ Nanoparticle/Polydopamine/Al₂O₃ Sandwich Structure for Complex Wastewater Treatment: Dynamic Catalysis Under Natural Light," *ACS Sustainable Chemistry & Engineering* 6 (2018): 8019.
108. Y. Yang, L. C. Yin, Y. Gong, et al., "An Unusual Strong Visible-Light Absorption Band in Red Anatase TiO₂ Photocatalyst Induced by Atomic Hydrogen-Occupied Oxygen Vacancies," *Advanced Materials* 30 (2018): 1704479.
109. J. Yan, T. Wang, G. Wu, et al., "Tungsten Oxide Single Crystal Nanosheets for Enhanced Multichannel Solar Light Harvesting," *Advanced Materials* 27 (2015): 1580.
110. W. J. Dong, J. W. Lim, D. M. Hong, et al., "Grain Boundary Engineering of Cu-Ag Thin-Film Catalysts for Selective (Photo)Electrochemical CO₂ Reduction to CO and CH₄," *ACS Applied Materials & Interfaces* 13 (2021): 18905.
111. J. Cheng, X. Yang, X. Xuan, N. Liu, and J. Zhou, "Development of an Efficient Catalyst With Controlled Sulfur Vacancies and High Pyridine Nitrogen Content for the Photoelectrochemical Reduction of CO₂ Into Methanol," *Science of the Total Environment* 702 (2020): 134981.
112. M. Kan, C. Yang, Q. Wang, et al., "Defect-Assisted Electron Tunneling for Photoelectrochemical CO₂ Reduction to Ethanol at Low Overpotentials," *Advanced Energy Materials* 12 (2022): 2201134.
113. S. Zhou, K. Sun, J. Huang, et al., "Accelerating Electron-Transfer and Tuning Product Selectivity through Surficial Vacancy Engineering on CZTS/CdS for Photoelectrochemical CO₂ Reduction," *Small* 17 (2021): 2100496.